IPP-Report

MAX-PLANCK-INSTITUT
FÜR PLASMAPHYSIK

Yu-Chih Liang

Simulations of the X-point Radiator in Tokamak Plasmas with the JOREK Code

IPP 2025-01
Januar 2025

MAX-PLANCK-INSTITUT
FÜR PLASMAPHYSIK

Simulations of the X-point Radiator in Tokamak Plasmas with the JOREK Code

Master's Thesis

For attainment of the academic degree of

Applied and Engineering Physics

submitted by

Yu-Chih Liang
<03775804>

in the School of Natural Sciences, Technical University of Munich

Supervision

Advisor: Prof. Dr. Ulrich Stroth

Assistance: Dr. Matthias Hoelzl, Dr. Andres Cathey

Submitted on October 01, 2024

Technical University of Munich, Arcisstraße 21, 80333 München, T: +49 (0)89-289-01, F: +49 (0)89-289-22000

Abstract

The problem of power exhaust in the future experimental thermonuclear fusion reactors, such as ITER and DEMO, necessitates operation regimes that can avoid extreme heat fluxes onto plasma-facing components. One promising regime is the X-point radiator (XPR), a cold, dense, and highly radiative plasma region that forms above the X-point of the single-null magnetic configuration in a tokamak plasma.

This thesis presents axisymmetric (2D) simulations of the XPR regime using the non-linear magnetohydrodynamic (MHD) code, JOREK, extended with a kinetic particle framework for neutral deuterium particles and impurities. The simulations explore the relationship between the XPR formation and phenomena like high-field-side high-density (HFSHD) formation and complete detachment. After a quasi-stationary XPR solution is achieved, various nitrogen seeding rates are tested to investigate the physical properties and stability of different XPR solutions.

Beside the quasi-stationary solution, this thesis presents two other simulations, one with the XPR moving vertically upwards and eventually turning into an unstable solution (MARFE) and the other with the XPR moving vertically downwards and eventually being lost. The two simulations show JOREK's capability of simulating time-varying XPR solution, and the analysis suggests sequences of physical effects that lead to the development of the XPR in these simulations.

The simulations presented in this thesis provide a solid baseline for future developments, particularly the transition to 3D simulations, so the MHD activities and their interaction with the XPR can be studied.

Contents

1 Introduction

1.1 Nuclear Fusion

Nuclear fusion is a process of combining two light nuclei into a heavier one. As the mass of the resulting nucleus is smaller than that of the combination of the starting ones, energy is released according to Einstein's mass-energy equation. Being able to control such process and harness fusion power is the ultimate goal in the field of fusion research. However, for both positively charged nuclei to fuse, they must be heated to extremely high temperature, namely having high kinetic energy, to overcome the Coulomb barrier and achieve large fusion reaction rate, which should be maximized for a commercial power plant. Currently, the most technologically feasible fusion reaction involves a deuterium and a tritium nucleus (D-T), as shown in (1.1), which has the highest reaction rates out of all the reactions at the order of 10 keV [1] [39].

$$\mathrm{D} + \mathrm{T} \rightarrow {}^{4}\mathrm{He}\,(3.5\ \mathrm{MeV}) + \mathrm{n}\,(14.1\ \mathrm{MeV}) \tag{1.1}$$

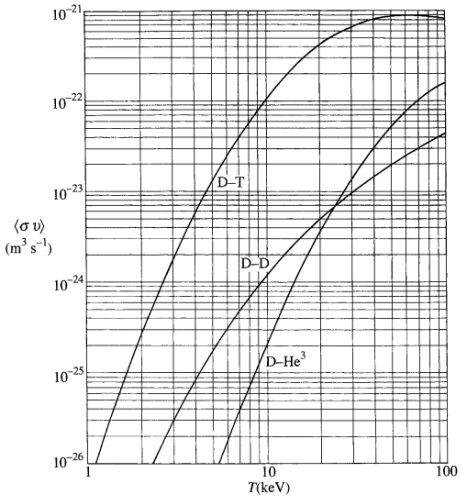

Figure 1.1: Reaction rates for different fusion reactions at ion temperature from 1 to 100 keV [39].

For stable power generation, the temperature of the D-T plasma should be self-sustained, namely maintained by the energy carried by the Helium nuclei, and no external heating is needed. Such a state of operation is called $ignition$, for which the product of density (n), temperature (T) and energy confinement time (τ_E) needs to exceed a certain value. This is known as the Lawson criterion [23], as shown in (1.2).

[1] $1eV \approx 11600K$

$$nT\tau_E > 3 \times 10^{21}\, m^{-3} \cdot keV \cdot s \tag{1.2}$$

To design fusion reactors, there are two main directions for plasma confinement: inertial confinement and magnetic confinement. The latter involves using a strong magnetic field to confine the fully-ionized gases along the field lines, which is the underlying principle for the fusion devices mentioned in this thesis.

1.2 Magnetic Confinement & Tokamaks

For magnetic confinement fusion (MCF) devices, there are mainly two concepts: tokamaks and stellarators. A tokamak has an axisymmetric geometry of a torus, as shown in figure 1.2, and its magnetic field has two main components: the toroidal field $\vec{B}_t$ and the poloidal field $\vec{B}_\theta$. $\vec{B}_t$ is generated by the toroidal field coils around the torus, and $\vec{B}_\theta$ is generated by the poloidal field coils and the toroidal plasma current I_p, where the latter is induced by the transformer coil at the center of the torus. Additionally, the vertical field coils create a field for plasma shaping and stability [39]. Combining these fields creates a helical $\vec{B}$. Since particles to the lowest order follow magnetic field lines, cross-field transport is low such that the plasma can be confined.

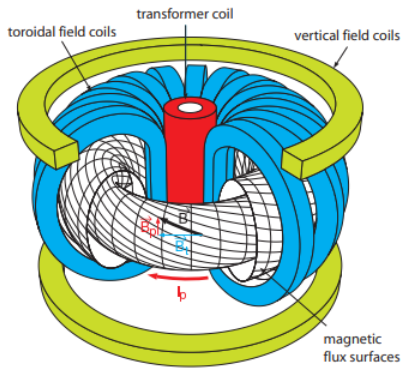

Figure 1.2: Scheme of the tokamak concept, adapted from figure 1.2 in [29].

On the other hand, a stellarator generates both $\vec{B}_t$ and $\vec{B}_\theta$ with the magnetic field coils and does not require a plasma current. In contrary to a tokamak, it is not an axisymmetric device. Stellarators are not within the scope of this thesis, so further details on them are not discussed.

The necessity of $\vec{B}_\theta$ comes from particle drifts. The shape of a torus helps to avoid end losses as one expects in a linear device, but then the toroidal field strength B_t is proportional to $1/R$ due to Ampère's law, with R being the major radius of the torus. This gradient of toroidal field strength and the curvature of toroidal field cause a particle drift in the direction of $\vec{B} \times \vec{\nabla} B$ (∇B-drift) for ions and the opposite for electrons, and the resulting charge separation creates a vertical electric field and eventually an $\vec{E} \times \vec{B}$ drift outward, sabotaging the confinement. Therefore, $\vec{B}_\theta$ is needed to allow a current along the helical field lines to short-circuit the

charge separation. Such current is called the Pfirsch-Schlüter current, and it is one of the essential building blocks for the tokamak concepts [39].

1.3 Magnetic Configuration

The magnetic configuration of a tokamak can be illustrated by the magnetic flux surfaces, which are nested layer-by-layer within the torus. On a given magnetic flux surface, the magnetic field lines wind helically and the plasma pressure stays constant. This is explained by the equilibrium condition (1.3), which requires the magnetic force to balance the plasma pressure force. From the equilibrium condition, the constant pressure along the field lines, hence constant on the flux surface, can also be explained (1.4), and any parallel pressure gradient is removed by the fast parallel (along $\vec{B}$) transport of the plasma [39].

$$\vec{j} \times \vec{B} = \vec{\nabla} p \tag{1.3}$$

$$\vec{B} \cdot \vec{\nabla} p = 0 \tag{1.4}$$

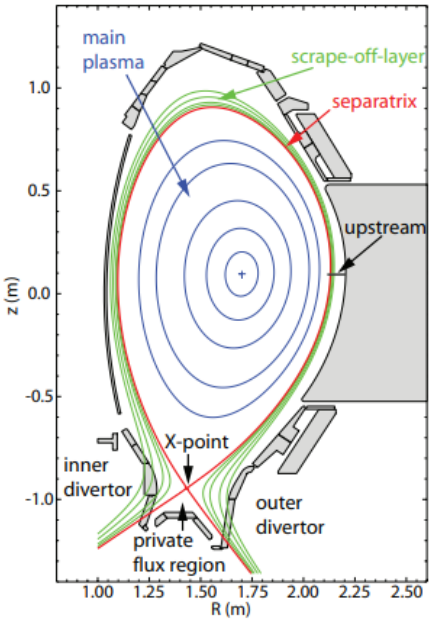

Figure 1.3: Poloidal cross section of flux surfaces in a lower single-null (SN) configuration in AUG, adapted from figure 1.3 in [29].

Figure 1.3 shows the poloidal cross-section of a magnetic configuration called the lower single-null (SN) divertor configuration in the ASDEX Upgrade (AUG) tokamak. In this configuration, additional coils below the divertors create a null point for the poloidal magnetic field, called the $X\text{-}point$. The separatrix separates the $confined\ region$ and the $scrape\text{-}off\text{-}layer$ (SOL). The confined region consists of closed flux surfaces that are not magnetically connected to the plasma facing components (PFC). In contrast, the SOL consists

of open flux surfaces that are magnetically connected to the $divertors$ or the PFC, meaning any plasma that escapes the confined region can travel along the field lines from the $upstream$ SOL to the divertors, via a $connection\ length\ L_c$ typically around 50 m in AUG.

The inner and outer divertor targets (IT/OT) are located on the $high\text{-}field\text{-}side$ (HFS) and $low\text{-}field\text{-}side$ (LFS), respectively, where HFS refers to the side closer to the center of the torus and with higher magnetic field strength ($B_t \propto 1/R$), and vice versa. The separatrix intersects with both targets at the $strike\ points$, and the strike lines separate the SOL and the $private\ flux\ region$ (PFR), which consists of open flux surfaces and is below the x-point in a lower SN configuration.

The upstream location is defined at the height of the magnetic axis, typically for SOL and closed flux surfaces near the separatrix. This location is also called the $inboard\ midplane$ (IMP) or $outboard\ midplane$ (OMP), depending on whether it is on the HFS or LFS, respectively. Especially on the OMP, the plasma profiles are often used for analysis due to the alignment of diagnostics.

1.4 High Confinement Mode

For different levels of confinement in tokamak operations, the operation regimes are categorized into the low confinement mode (L-mode) and the high confinement mode (H-mode). The H-mode was discovered in the ASDEX tokamak and was found to have an increased energy confinement time by a factor of two comparing to the L-mode [38]. When the heating power exceeds a threshold, the plasma abruptly transitions from L-mode to the H-mode regime. Although detailed mechanisms for such transition are not yet fully understood, the main reasoning for the L-H transition is often referred to the creating of a strong $E \times B$ shear flow in the plasma edge. Such shear flow reduces turbulent transport, which is the main contributor to plasma escaping the confined region in L-mode, so its location is also called the edge transport barrier, as shown in figure 1.4.

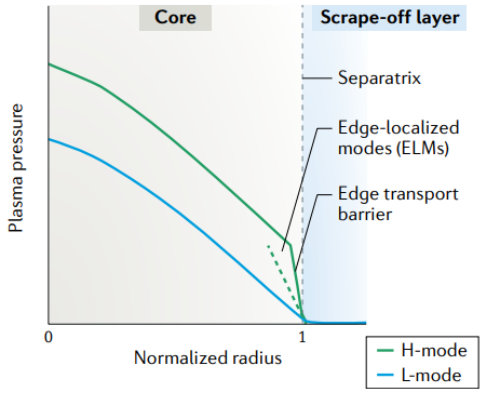

Figure 1.4: Typical OMP plasma pressure profiles in H-mode and L-mode, adapted from Box 1 figure b in [14].

The transport barrier helps to build up a large pressure gradient right inside the separatrix, and this region

is called the $pedestal$, a feature in H-mode that allows the plasma core to develop higher temperature and density. After discovery, the H-mode has been realized in other tokamaks and has become the standard operation regime due to the enhanced confinement performance. Additionally, there exists the I-mode and more detailed classification of the H-mode, but only the standard H-mode is discussed in this thesis.

In a standard H-mode regime, as the plasma pressure at the pedestal top builds up, an increased pressure gradient in the plasma edge can lead to magnetohydrodynamic (MHD) instabilities, which relaxes the pedestal pressure as shown the dashed line in figure 1.4. Such relaxation takes place in hundreds of microseconds up to a few milliseconds and is called an $edge\ localized\ mode$ (ELM) [40]. It repetitively causes the plasma to escape confinement and enter the SOL, increasing the particle and heat loads onto the divertor targets.

1.5 Power Exhaust Problem in Future Reactors

As larger fusion reactors are being designed and built to reach the ignition condition, such as ITER and DEMO, the heat flux due to large ELMs (such as type-I ELMs [40]) could exceed the peak heat flux limit of the divertor targets (5 MW/m^2) and erode the tungsten. Therefore, for ITER [9], DEMO [41] and other power-plant relevant fusion reactors, ELMs are dangerous and have to be avoided. Furthermore, even in the absence of such large transient event, there has to be a reliable mechanism for the plasma escaping confinement to exhaust its energy before reaching the divertor targets [11]. Namely a $detached$ regime, where the heat flux and particle flux onto the divertors are greatly reduced, will need to be maintained during a continuous operation of a reactor plasma [30]. Further details on the process of detachment are described in section section 2.1.2.

1.6 The X-point Radiator & Research Questions for the Thesis

This thesis is focused on one of the potential solutions to the power exhaust problem: The X-point radiator (XPR). The XPR is a plasma volume located above the x-point inside the confined region that is cold, dense and highly radiative. Such properties allow it to buffer the heat exhaust and protect the PFC. Therefore, the XPR regime is inherently detached and can even be controlled to reach an ELM-suppressed regime [2]. The theory for the physics and the experimental observation of the XPR regime are discussed further in chapter 2.

The aim of the thesis project is to conduct axisymmetric (2D) simulations of the XPR using the MHD code JOREK [17] with its kinetic particle extension for neutrals and impurities [20]. Further details about JOREK are given in chapter 3. Essentially, the simulations aim to answer the following research questions:

- How does XPR formation relate to other phenomena, such as high-field-side high-density formation and detachment, that also heavily involve neutral particle physics?
- What are the main mechanisms that drive the vertical development of the XPR?
- Can time evolutions into and out of the XPR regime be simulated?

- What are the physical properties of an unstable XPR?

In chapter 4, the XPR formation is demonstrated, with the high-field-side high-density formation and detachment both present in the same simulation. Then the XPR solution is maintained quasi-stationary in order to study its physical properties.

At a certain time point of the quasi-stationary solution, the input parameters of the simulation are varied, and two other solutions branch out. One leads to a strongly developing XPR, for studying the stability of the solution. The other one leads to a gradually lost XPR, for studying the physical mechanisms behind a retreating XPR. In chapter 5, the analysis on the two other solutions is presented.

Lastly, the conclusion summarizes the findings and provides an outlook on the potential future work that can be extended from this thesis project.

2 The X-point Radiator Regime

2.1 The Effects of Gas Puffing

In AUG, gases can be directly puffed from the private flux region (PFR) or the outer midplane (OMP), as shown in figure 2.1. In this thesis, the relevant gases are deuterium and nitrogen. In the case of deuterium being the main plasma species, the puffed deuterium builds up density, so the rate of deuterium fueling is called the "fueling rate" with the unit e^-/s. Nitrogen is an impurity that effectively cools the divertor and leads to detachment [19]. The rate of nitrogen seeding is also expressed with the same unit e^-/s [1] as the unit.

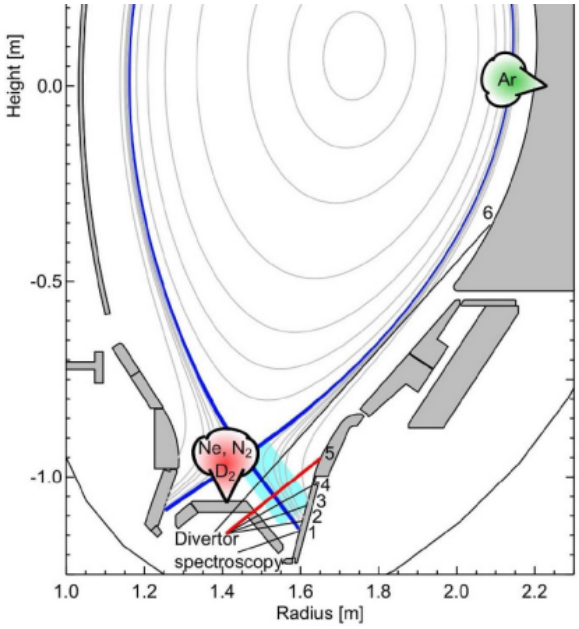

Figure 2.1: Gas valve locations for puffing different types of gasses with the magnetic configuration and the lines of sight (LOS) of divertor spectroscopy, adapted from figure 2 (a) in [15].

2.1.1 High-field-side high-density formation

One effect from the deuterium gas fueling is the formation of the high-field-side high-density (HFSHD) front, which is an effect of increased plasma density at the HFS scrape-off-layer (SOL), both near the

[1] The unit e^-/s is used for both fueling and seeding rates so that the two quantities can be in the same order of magnitude, allowing easier comparison in the same plot. If were to convert to atoms/s, the seeding rate would need to be divided by 7, the atomic number of nitrogen.

HFS target and upstream at the inner midplane (IMP). HFSHD formation happens when there is magnetic connection between HFS and LFS SOL, namely between the primary and secondary separatrices, as shown in figure 2.2 [13].

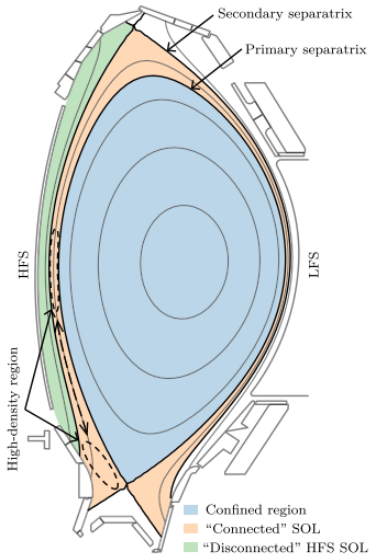

Figure 2.2: Illustration of SOL that are connected (orange) or disconnected (green) between HFS and LFS, adapted from figure 3 in [13].

2.1.2 Detachment

Impurities can more rapidly dissipate heat via line radiation than deuterium can, so introducing nitrogen seeding can lead to complete detachment. To briefly describe the stages of detachment, a divertor target gets partially detached before getting completely detached. As a divertor target is partially detached, the temperature at the target and the ion flux onto the target are reduced, and the parallel pressure along the SOL is reduced near the strike point. As a divertor target is completely detached, the profiles of temperature and ion flux are strongly flattened along the target, and the parallel pressure gradient develops larger and further upstream [30]. Such description can be used for the detachment of both H-mode and L-mode plasma [31].

Additionally, in a lower single-null configuration with the ion ∇B-drift pointing from the plasma core to the x-point, the inner target (IT) gets detached before the outer target (OT) does [31]. This asymmetry of degree of detachment is due to plasma drifts [21], which is shown in figure 2.3. Further details on plasma drifts are given in section section 2.2.1. Lastly, upon complete detachment on both targets, the HFSHD also disappears [5].

To sum up, the process of detachment can be described as such: HFSHD formation & partially detached IT $\mapsto$ completely detached IT $\mapsto$ partially detached OT $\mapsto$ completely detached OT & loss of HFSHD front.

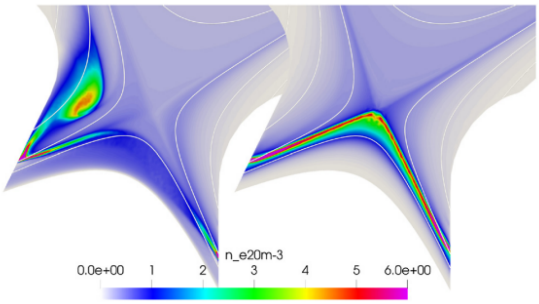

Figure 2.3: 2D plot of electron density n_e in a JOREK simulation for detachment with (left) and without (right) plasma drifts, adapted from figure 16 in [21].

2.1.3 X-point radiator formation

In a state of pronounced detachment, the regions of strong impurity line radiation can move from the divertor targets to the vicinity of the x-point, which corresponds to the formation of the X-point radiator (XPR). The XPR exists inside the confined region and can develop further inward [2]. Such development and XPR control are discussed further in section 2.4. Figure 2.4 shows AUG discharge #29383 with nitrogen seeding and compares the radiative power density (P_{rad}) between a time window without (1.85 s) and with (3.90 s) an XPR. XPR formation also corresponds to an increase of the total radiative power fraction ($f_{rad} = P_{rad,tot}/P_{heat}$) from 50 $\sim$ 60 % to 80 $\sim$ 90 % in this discharge, with N_{III} and Balmer line radiation dominating in the XPR region [31]. Additionally, for AUG, the phenomenon of XPR can be consistently reproduced in discharges that reach a detached condition with nitrogen, whilst the total heating power is varied over a wide range (2.5 MW $\leq P_{heat} \leq$ 20 MW) [2].

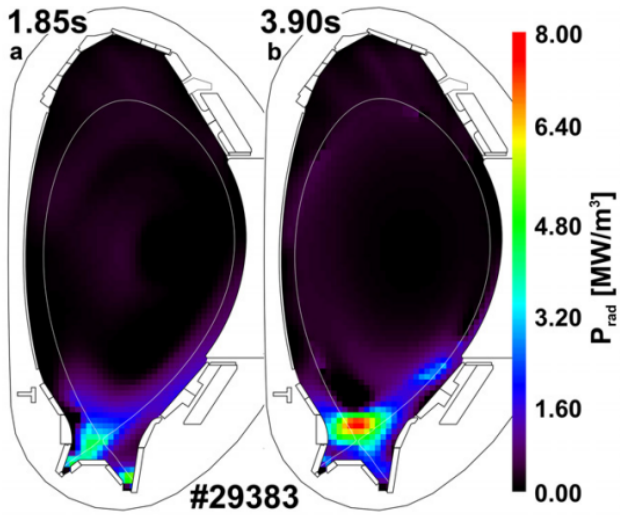

Figure 2.4: Tomography of bolometer measurements before (1.85 s) and after (3.90 s) nitrogen seeding with the indication of separatrix from magnetic reconstruction, adapted from figure 6 in [31].

An XPR is related to another phenomenon called multifaceted asymmetric radiation from the edge (MARFE)

[24]. Both are toroidally symmetric highly radiative regions. The toroidal symmetry of an XPR is shown by the visible light camera image in figure 2.5. Additionally, they are both strong power sinks, and their development can be explained by radiation condensation, which is a process of strong radiation leading to a local decrease in the plasma temperature and an increase in plasma density to maintain the pressure balance [10]. The major difference between XPR and MARFE is that an XPR can be kept stable, whilst a pressure hole can form inside a MARFE, which then drifts further into the plasma core and causes disruptions [2]. However, if an XPR is not kept in the stable regime, it can still turn into a MARFE. The detailed description of such development is discussed in section 2.3.3.

Figure 2.5: Visible light camera image of an XPR in AUG discharge (#40007) at 3.4 s, showing the blue light above the x-point mainly from N^{2+} and the red light of Balmer radiation at the divertor legs, adapted from figure 1 in [3].

2.2 Impurity Transport

As nitrogen particles are introduced to the system from the private flux region (PFR) and get ionized into any given charge state, they are subject to magnetic confinement along the magnetic field lines like the background plasma (ionized deuterium) is. However, there exist three dominant mechanisms responsible for the cross-field transport of impurities: the $E \times B$ drift, collisional neoclassical transport and in the axisymmetric mean field, the transport induced by 3D instabilities. With such transport mechanisms, impurities can travel across the separatrix and dilute the main plasma. On one hand, this then leads to the formation of the XPR and helps with the power exhaust problem. On the other hand, an increased impurity concentration in the main plasma can lead to a degradation of energy confinement in the plasma edge and core [2].

2.2.1 $E \times B$ drift

As shown in equation (2.1), an electric field perpendicular to the magnetic field lines causes both positively and negatively charged particles to drift in the $\vec{E} \times \vec{B}$ directions.

$$\vec{v}_{E\times B} = \frac{\vec{E} \times \vec{B}}{B^2} \tag{2.1}$$

Such cross-field transport can be either along or perpendicular to flux surfaces. Namely a radial (i.e. along the minor radius) electric field (E_r) creates a poloidal drift and a poloidal electric field (E_θ) creates a radial drift. For example, in an XPR simulation with the 2D transport code SOLPS-ITER [28], the poloidal component E_θ points outward from the x-point and the radial component E_r is large in the highly ionizing region, as shown in figure 2.6.

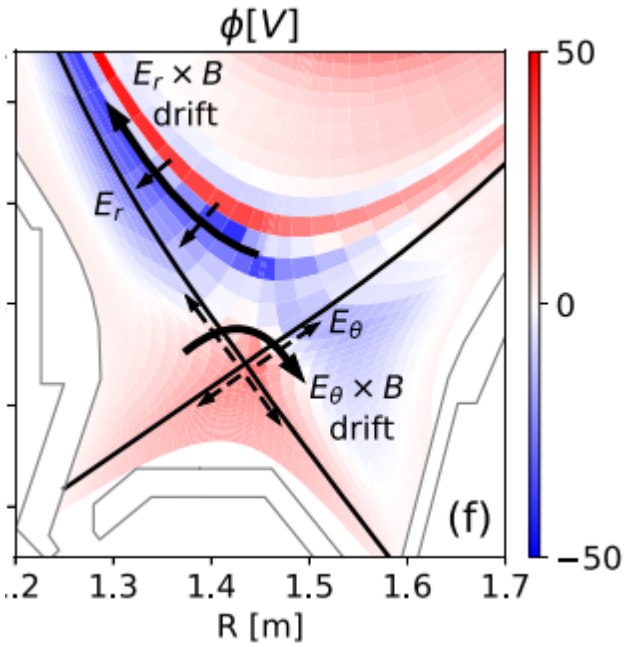

Figure 2.6: 2D plot of electric potential in a SOLPS-ITER XPR simulation (direction of $\vec{B}$ is out of plane/ ∇B-drift points from plasma core towards the x-point/ favorable configuration), adapted from figure 11 (f) in [28].

E_θ creates the drift around the x-point, responsible for transporting the nitrogen from the PFR to HFS SOL, then towards the XPR region. The potential hill at the x-point relates to currents leaving the x-point that are driven by ∇B-drift [32].

On the other hand, E_r creates the poloidal drift that is responsible for transporting the nitrogen in the XPR region further upstream on the HFS. The potential well relates to the locally strong ionization [28].

2.2.2 Collisional neoclassical transport

In the classical transport theory, perpendicular transport is dominated by small-angle Coulomb collisions between ions and is only influenced by local quantities. In the neoclassical transport theory, the global geometry of the inhomogeneous and curved magnetic field lines is taken into account and found to be strongly influential to perpendicular transport [1]. In the context of impurity transport, the nitrogen ions can have collisions among themselves or with the deuterium ions, enhancing the cross-field transport. This effect helps the nitrogen ions to diffuse from the PFR to the SOL, crossing the separatrix and entering the

confined region.

The detailed neoclassical transport theory is not further discussed as it is not the focus of the thesis, but how this effect is modeled is discussed in section 3.2.

2.3 XPR model

A reduced model for XPR formation [35] can be derived by analyzing the power balance within a simplified geometry, which includes the XPR region and the flux tube that connects it to upstream on the LFS. Detailed information about the flux tube geometry is introduced in section 2.3.1. The power balance between parallel heat conduction into the XPR region and the power losses via atomic processes is used to derive the access parameter of the XPR, which is discussed in section 2.3.2. Lastly, by considering recombination in the cold XPR core, the particle balance between the parallel particle transport and recombination losses is used to derive the MARFE occurrence parameter, which is discussed in section 2.3.3.

2.3.1 Simplified geometry for the flux tube analysis

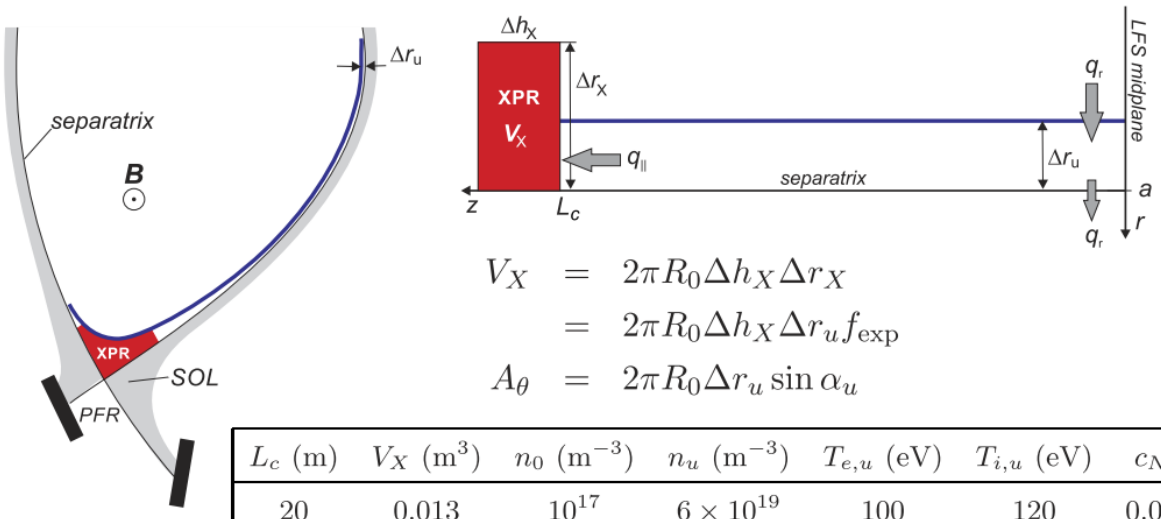

$$V_X = 2\pi R_0 \Delta h_X \Delta r_X = 2\pi R_0 \Delta h_X \Delta r_u f_{\exp}$$

$$A_\theta = 2\pi R_0 \Delta r_u \sin \alpha_u$$

L_c (m)	V_X (m^3)	n_0 (m^{-3})	n_u (m^{-3})	$T_{e,u}$ (eV)	$T_{i,u}$ (eV)	c_N
20	0.013	10^{17}	6×10^{19}	100	120	0.01

Figure 2.7: Left: geometry of the flux tube and the XPR volume. Right: simplified geometry for power and particle balances, adapted from figure 1 in [35].

Figure 2.7 shows the geometry of the reduced model. The red region is defined as the XPR volume, and the flux surface marked in blue is the upper bound of the XPR. Between the flux surface and separatrix, the flux tube is assumed to have a constant width of Δr_u and a length of the connection length L_c, and the XPR volume V_X is calculated with equation (2.2), where R_0 is the major radius at the XPR, Δh_X is the horizontal extension of the XPR and the radial extension Δr_X can be calculated from the flux expansion $f_{exp} = \Delta r_X / \Delta r_u$.

In the next sections, the following geometric parameters are used for a typical XPR in AUG: $\Delta r_u = 1$ mm, $L_c = 20$ m, $R_0 = 1.65$ m, $f_{exp} = 25$ and $\Delta h_X = 5$ cm. The resulting XPR volume is $V_X \approx 0.013$ m^3. V_X is then used for the calculation of volumetric processes (ionization, recombination, charge exchange and impurity line radiation) [35].

$$V_X = 2\pi R_0 \Delta h_X \Delta r_u f_{exp} \tag{2.2}$$

Additionally, the effective poloidal area of the XPR, A_θ, is calculated with equation (2.3), where the magnetic pitch angle α_u is estimated with safety factor $q_s = B_\varphi a / B_\theta R_0$ in equation (2.4). The resulting poloidal area is $A_\theta \approx 0.00104$ m^2. A_θ is then used for the calculation of parallel particle and power flux from the flux tube into the XPR [35].

$$A_\theta = 2\pi R_0 \Delta r_u \sin \alpha_u \tag{2.3}$$

$$\sin \alpha_u = \frac{B_\theta}{B} \approx \frac{B_\theta}{B_\varphi} \approx \frac{a}{R_0 q_s} \tag{2.4}$$

2.3.2 XPR access condition

The following assumptions are made for the power balance within the flux-tube-XPR system [35]:

- The upstream quantities are fixed.
- Parallel heat conduction $q_\parallel$ from upstream to XPR is the only heat source for the XPR volume and is constant.
- Only electron heat conduction is taken into account as the ion heat conductivity is about 60 times lower than that of electrons due to the electron-ion mass ratio.
- Radial heat flux from the core q_r through the flux tube maintains the upstream electron temperature.
- Three volumetric processes serve as power sink in the XPR volume: electron-impact ionization of neutral deuterium, charge exchange (CX) processes and impurity line radiation [33].
- Radial transport in the XPR is neglected.
- In the XPR volume, ion and electron temperatures are identical ($T_{i,X} = T_{e,X} = T_X$).
- In the XPR volume, coronal equilibrium is assumed.

As shown in figure 2.8, electron-impact ionization of deuterium neutrals and CX between deuterium ions and neutrals are firstly responsible for cooling the XPR down to $T_X \approx 20$ eV, where nitrogen line radiation becomes dominant and further cools it down to around $1eV$.

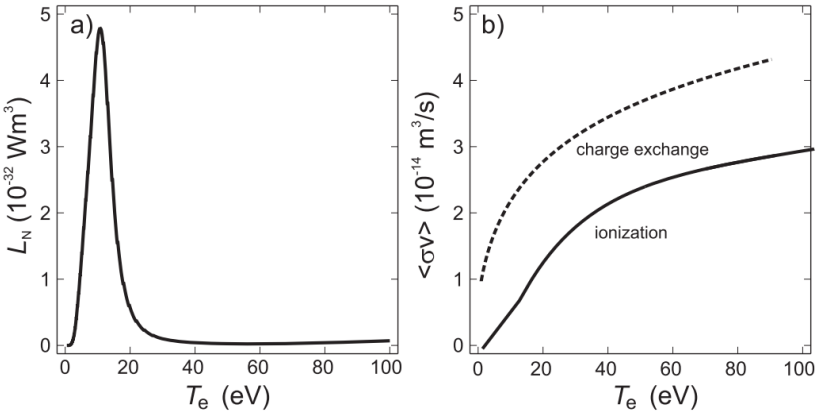

Figure 2.8: (a) Line radiation curve for nitrogen and (b) rate coefficients for electron-impact ionization and CX processes for deuterium, adapted from figure 2 in [35].

The power source and sink terms for the XPR are estimated for electron parallel heat conduction (2.5), electron-impact ionization (2.6), CX processes (2.7) and nitrogen line radiation excitation (2.8) according to [35]. In the equations, $\hat{\kappa}_e = 1820$ W(eV$^{7/2}$ m)$^{-1}$ from equation (16.10) in [34]. $T_u \approx (T_{e,u} + T_{i,u})/2$ and n_u are the upstream temperature and density, respectively. For the quantities in the XPR volume, n_0 is the neutral deuterium density. n_X is the deuterium ion density, c_N is the nitrogen concentration and $L_N(T_{e,X})$ is the emission coefficient [26] for nitrogen line radiation depending on the local electron temperature. Also, n_X can be calculated from the kinetic pressure ($p_{kin} = n_i T_i + n_e T_e$) being constant along the flux tube, resulting in equation (2.9).

$$P_{cond,e} = A_\theta q_\parallel \approx A_\theta \frac{2\hat{\kappa}_e}{7L_c} T_u^{\frac{7}{2}} \tag{2.5}$$

$$P_{ion} \approx 2 \langle \sigma v \rangle_{ion} n_u n_0 T_u V_X \tag{2.6}$$

$$P_{cx} \approx \langle \sigma v \rangle_{cx} n_u n_0 T_u V_X \tag{2.7}$$

$$P_{rad} = L_N(T_{e,X})\, n_X^2 c_N V_X \sim n_X^2 c_N f_{exp} \tag{2.8}$$

$$n_X = \frac{T_{e,u} + T_{i,u}}{T_{e,X} + T_{i,X}} n_u \tag{2.9}$$

Given the following parameters typical for AUG: $n_u = 6 \times 10^{19}$ m^{-3}, $T_u = 110$ eV, $n_0 = 10^{17}$ m^{-3} and $c_N = 1$ %, the power source and sink terms are shown in figure 2.9 (a). The intersections of total power loss and heat conduction make three solutions to the power balance. Of the stable solutions, one is high-temperature (≈ 80 eV) and the dominant power loss mechanisms are ionization and CX. The other is low-temperature (≈ 1 eV) and the dominant power loss mechanism is nitrogen line radiation. The latter

indicates the formation of an XPR [35]. In the unstable solution ($\approx$ 20 eV), any change of local temperature leads to a bifurcation towards either the high-temperature or low-temperature solution.

In figure 2.9 (b), the residuum of the power balance (2.10) is calculated for $n_0 = 3 \times 10^{17}$ m^{-3}, 10^{17} m^{-3} and 10^{16} m^{-3}. As ionization and CX power losses both scale with n_0, the increase of neutral density causes the high-temperature solution to eventually vanish, and the only remaining stable solution is the XPR. This indicates that n_0 is the key parameter regarding XPR formation [35].

$$P_{res} = P_{rad} + P_{ion} + P_{cx} - P_{cond,e} \tag{2.10}$$

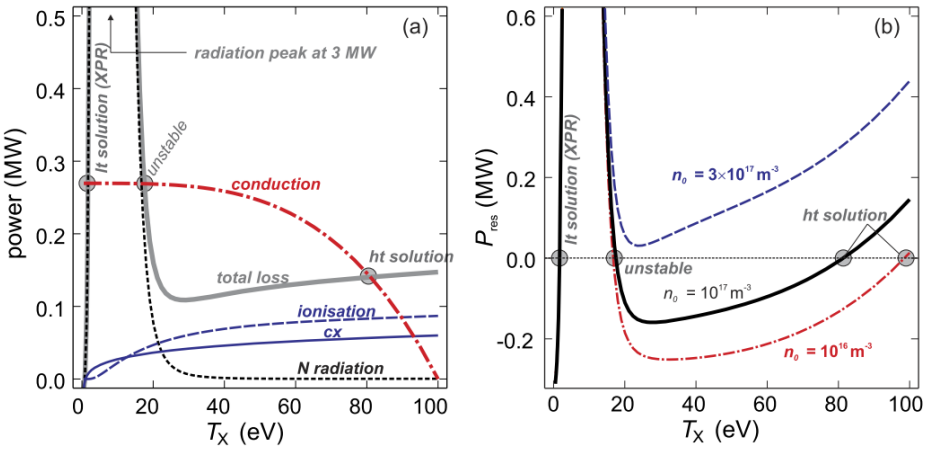

Figure 2.9: (a) Power source and sink terms with respect to electron temperature in the XPR. The total power loss intersects with heat conduction and forms one high-temperature, one unstable and one low-temperature solution (b) Residuum power P_{res} with various values of n_0, adapted from figure 3 in [35].

Since P_{rad} is negligible for the high-temperature solution, the access condition for the XPR solution can then be derived from the criterion $P_{ion} + P_{cx} > P_{cond,e}$, and the resulting scaling expression of the XPR access parameter X_A is shown as equation (2.11) [35].

$$X_A \sim \frac{R_0^2 q_s^2 f_{exp}}{a} \frac{n_u n_0}{T_u^{\frac{5}{2}}} \tag{2.11}$$

2.3.3 MARFE occurrence parameter

For the stability of XPR, namely if it develops into a MARFE, the low-temperature solution is studied. The particle balance in the XPR volume is thus analyzed with the conditions of the cold and strongly radiating XPR core:

- At the typical XPR temperature $T_X \approx 1$ eV, the dominant mechanism for the particle sink is recombination.

- Only parallel particle transport from upstream is considered as the particle source in the XPR core. Radial transport is assumed to be much weaker than parallel transport.
- For parallel transport, convection with ion sound speed is assumed. Additionally, entering the cold plasma volume, supersonic flows can be present [12], but this is not taken into account in the model.
- Ionization is also neglected as the temperature is very low in the XPR core. However, an extension to the model could be to include the ionization source outside the XPR core [35].
- Kinetic pressure p_{kin} does not stay constant along the flux surface through the XPR core.
- Total pressure $p_{tot} = p_{kin} + p_{dyn}$ should be considered, with $p_{dyn} = m_i n_i v_\parallel^2$ being the dynamic pressure from the parallel flow $v_\parallel$.

The particle source and sink terms for the XPR core are calculated for parallel transport (2.12) and recombination rate (2.13). If the particle balance can be maintained ($\Gamma_{in} = \Gamma_{rec}$), p_{tot} remains constant along the flux surface through the XPR core ($2n_X T_X + m_i n_X v_\parallel^2 = 2n_u T_u$). Assuming the ion sound speed being the parallel flow velocity ($v_\parallel = c_{s,i} = (2T_X/m_i)^{1/2}$) in the XPR core, no friction between plasma flow in the ionization region and no viscous effects, the total pressure balance leads to equation (2.14) [33], relating the upstream and XPR quantities [2].

$$\Gamma_{in} = A_\theta c_s n_X \tag{2.12}$$

$$\Gamma_{rec} = n_X^2 \langle \sigma v \rangle_{rec} V_X \tag{2.13}$$

$$n_X = \frac{T_u}{2T_X} n_u \tag{2.14}$$

If the particle balance cannot be maintained ($\Gamma_{rec} > \Gamma_{in}$), conservation of p_{tot} along the flux surface is broken, and a pressure hole in the XPR core develops. Due to the diamagnetic effect, the pressure hole drifts towards the HFS, in contrast to a plasma blob in the SOL, which drifts towards the opposite direction [35]. Such a transition to the non-stationary pressure hole can be characterized as the development from a stable XPR solution to a MARFE. Combining equations (2.12), (2.13), (2.14), and assuming $T_u = T_{i,u} = T_{e,u}$, the inequality $\Gamma_{rec} > \Gamma_{in}$ leads to (2.15), which can be used to calculate the T_X under which a MARFE develops.

$$\frac{\langle \sigma v \rangle_{rec}(T_X)}{T_X^{3/2}} > \sqrt{\frac{2}{m_i}} \frac{A_\theta}{V_X} \frac{2}{n_u T_u} \tag{2.15}$$

In the low-temperature solution, the power balance is between the impurity line radiation power (2.8) and the conducted power (2.5), as ionization and CX losses are weak in such low temperature. Assuming $T_X \ll T_u$ and using (2.9), equation ($P_{rad} = P_{cond,e}$) leads to (2.16), which can be used to calculate T_X.

$$\frac{L_z(T_X)}{T_X^2} = \frac{T_u^{3/2}}{n_u^2} \frac{2\hat{\kappa_e} A_\theta}{7 L_c V_X} \frac{4}{c_{imp}} \tag{2.16}$$

[2] Note that (2.14) differs from (2.9). The latter is derived from the conservation of kinetic pressure.

Combining equations (2.15) and (2.16), the scaling expression for the MARFE occurrence parameter is derived as (2.17). Given a fixed magnetic geometry and upstream parameters, M_A scales with c_{imp}, meaning that the increase in impurity concentration in the XPR volume reduces T_X until the XPR core is cold enough to turn into a MARFE.

$$M_A = \frac{R_0^3}{a^2}\sqrt{\frac{m_i}{T_u}} n_u^3 q_s^3 f_{exp}^2 c_{imp} \tag{2.17}$$

2.4 XPR Control & ELM Suppressed Regime

Experimentally, the development of XPR, in terms of vertical position with respect to the x-point, can be controlled by two physical parameters: total heating power and impurity seeding rate [2]. The top two plots in figure 2.10 show a strong correlation between the nitrogen seeding rate and the XPR position, and the nitrogen seeding rate can be feedback controlled in order to develop the XPR position to the pre-set value. As the XPR can be controlled up to 10 cm above the x-point in AUG experiments, the total radiated power fraction $f_{rad} = P_{rad,tot}/P_{tot}$ increases to about 100 %, meaning that less power needs to be exhausted at the divertor targets, which is a great feature of the XPR regime for the power exhaust problem. Furthermore, in AUG discharge #36655, it is observed that ELMs disappear when the XPR position is around 7 cm above the x-point [2], which is the time frame marked green in the upper plot of figure 2.10.

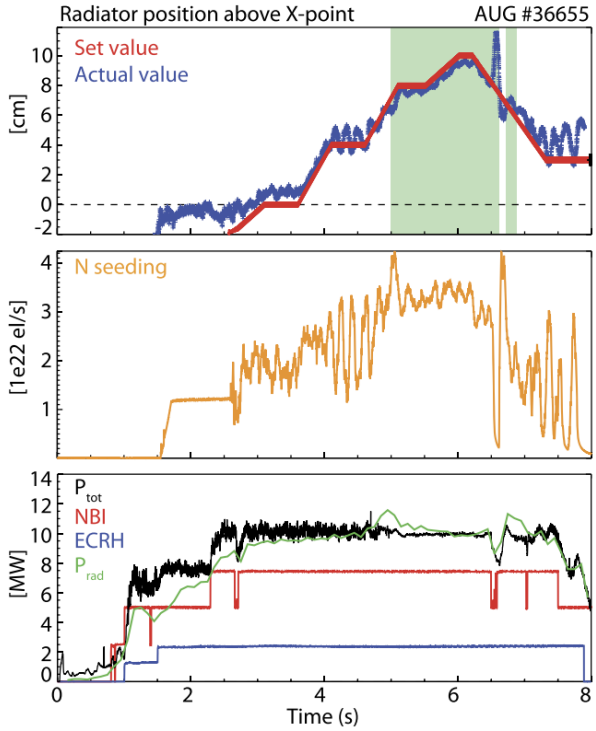

Figure 2.10: XPR control for AUG discharge #36655 with N seeding rate feedback-controlled by real-time measurements of XPR position. The bottom plot shows the total heating power P_{tot} and total radiated power $P_{rad,tot}$, and the ELM-suppressed regime is marked green in the top plot, adapted from figure 5 in [2].

3 The JOREK Code

3.1 Reduced MHD Model

JOREK is a non-linear extended MHD code for simulating fusion plasmas in a realistic Tokamak geometry [7, 16–18], with various extensions currently being developed. JOREK can be used to study large-scale plasma instabilities, particularly focusing on modeling plasma edge phenomena, SOL physics and disruptions. Additionally, with the kinetic particle framework, a simplified JOREK XPR simulation has been firstly attempted and achieved [36]. For the purpose of this thesis, details regarding the full MHD model, the technicalities and different extensions are not explained and the reader is referred to [16, 17, 20, 37]. Instead, only the relevant model with features and extensions used within the scope of the thesis project are listed below and elaborated:

- Reduced MHD model with single temperature ($T_i = T_e$) and diamagnetic extension.
- Perfectly conducting wall boundary condition.
- Grid-to-wall extension.
- Kinetic neutrals and impurities framework (discussed in section 3.2).

Symbol	Description	
Ψ	Poloidal magnetic flux	$= R\mathbf{A} \cdot \mathbf{e}_\phi$ with $\mathbf{A}$ the vector potential
u	Velocity stream function	$= \Phi/F_0$ with Φ the electric potential
j	Toroidal current density	$= -R\mathbf{j} \cdot \mathbf{e}_\phi = \Delta^* \Psi$
ω	Toroidal vorticity	$= \Delta_{\mathrm{pol}} u$
ρ	Mass density	$= n_\mathrm{e} m_\mathrm{ion}$ for singly charged ions
T	Temperature	$\equiv T_\mathrm{e} + T_\mathrm{i}$ in the single temperature model
$v_\parallel$	Parallel velocity	$= \mathbf{v}_\parallel \cdot \mathbf{B}/B^2$

Figure 3.1: Physical variables in the JOREK reduced MHD model, adapted from Table 1 in [17].

An ansatz-based approach for the reduced MHD model is used in JOREK, which neglects changes in $\vec{B_\phi}$ and assumes that the time-dependent part of magnetic vector potential $\vec{A}$ is dominated by the toroidal component, leading to the ansatz for the magnetic field (3.1), with the normalized toroidal basis vector $\vec{e_\phi}$. By approximating $\vec{B_\phi}$ with the vacuum toroidal field F_0/R, meaning a constant F_0 instead of $F(\Psi)$ is used, toroidal field compression is neglected, which usually only matters for internal kink studies [27], and fast magnetosonic waves are eliminated. Furthermore, the magnetic vector potential can then be defined by one

scalar function (Ψ) [17].

$$\vec{B} = \frac{F_0}{R}\vec{e_\phi} + \frac{1}{R}\vec{\nabla}\Psi \times \vec{e_\phi} \Rightarrow \vec{A} = \Psi\vec{\nabla}\phi \tag{3.1}$$

From (3.1), velocity can then be approximated as (3.2), where $\delta^* = m_i/\left(eF_0\sqrt{\mu_0 n_0 m_i}\right)$ is the diamagnetic coefficient. This approximation includes the $E \times B$ drift velocity $\vec{v}_{E\times B}$, ion diamagnetic drift velocity $\vec{v}_{dia,i}$ and flows along the magnetic field lines $\vec{v}_\parallel$. Also, the velocity field can be defined by two scalar functions (u and $v_\parallel$) [17].

$$\vec{v} = \vec{v}_{E\times B} + \vec{v}_{dia,i} + \vec{v}_\parallel = -R\vec{\nabla}u \times \vec{e_\phi} - \delta^* R\frac{\vec{\nabla}\left(\rho T_i\right)}{\rho} \times \vec{e_\phi} + v_\parallel \vec{B} \tag{3.2}$$

Using only three variables to define $\vec{A}$ and $\vec{v}$, the reduced model requires less computational cost and allows larger simulation time steps comparing to the full MHD model. The typical temporal resolution is of the same order of magnitude of the Alfvén time $t_A = a\sqrt{\mu_0 n_0 m_i}/B_0$ ($\sim \mu s$) [1]. For the simulations shown in this thesis, the time is normalized to $\Delta t_{fluid} = 2.2786\ \mu s$.

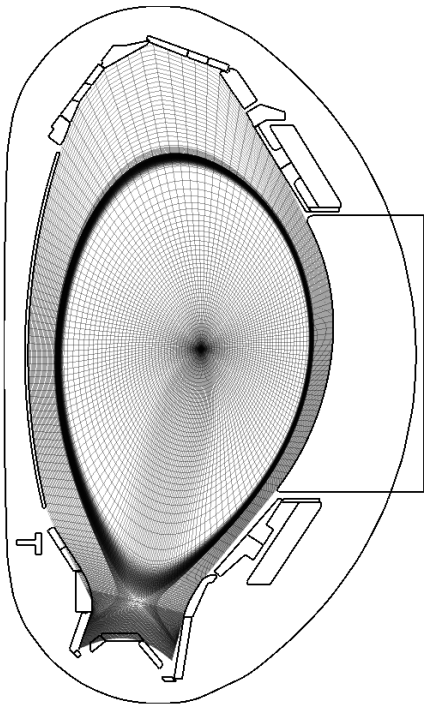

Figure 3.2: Flux-aligned grid with grid-to-wall extension to the ASDEX Upgrade first wall.

For the spatial discretization, JOREK solves the equations on a 2D Bézier finite element grid on the poloidal plane, combined with a toroidal Fourier expansion [7, 17] [2]. In the beginning of a simulation, a polar grid is

[1] μ_0 is the vacuum permittivity; n_0 and B_0 are the plasma number density and magnetic field strength at the plasma center, respectfully.

[2] Only axisymmetric (2D) simulations are shown in this thesis. The toroidal Fourier harmonics with specified mode numbers are required for studying instabilties, which is beyond the scope of the project.

used to solve the Grad-Shafranov equilibrium, which is used to generate a flux-aligned grid with the x-point geometry. Figure 3.2 shows an ASDEX Upgrade setup for which the flux aligned grid is extended to the first wall (FW), including the far SOL region in the computational domain. The FW is assumed perfectly conducting, meaning Ψ and j are fixed at the computational boundary.

3.2 The JOREK Kinetic Particle Framework

Coupled to the base reduced MHD model, the kinetic particle framework is used to model neutral particles and impurities [37]. In this framework, particles are pushed with the Boris method [4] through the background electric field and magnetic field, gyrating due to Lorentz force if they are charged, and the full orbits are followed in real space (R,Z,ϕ) coordinates with correction for the toroidal geometry [8].

The particle framework tracks the computational particles (superparticles) with the Monte-Carlo method, and a full-f approach is followed. For further details of the framework, the reader is referred to [37]. For either neutrals or impurities, each superparticle carries all necessary quantities: weight, position, mass of the species, velocity and charge state [3], and the number of superparticle (n_particles) can typically be kept at around 10^7. For the simulation shown in this thesis, a maximum of 2×10^7 is set for n_particles. Then superparticles of the same species belong to a group, which contains the mass of the species and the list of superparticles. Figure 3.3 shows a flowchart of the particle loop and how it is two-way coupled to the background MHD field. In the particle loop, the atomic physics for both species is calculated with the reaction rate coefficients [26] included in the framework.

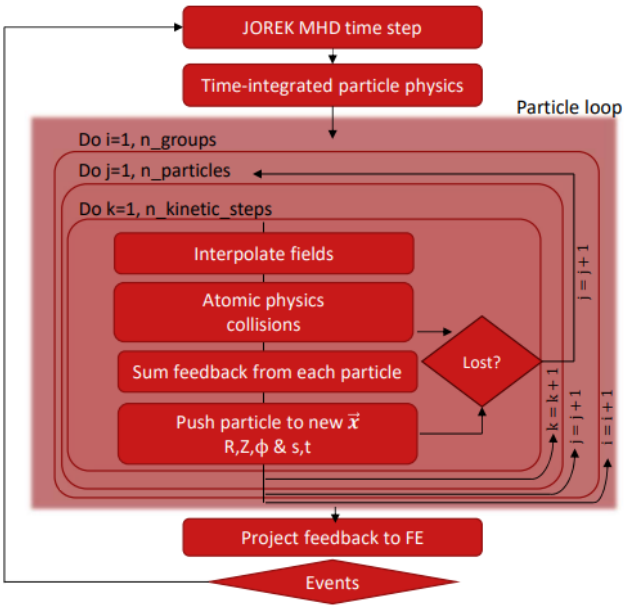

Figure 3.3: Flowchart for the particle loop within one MHD (fluid) time step Δt_{fluid}, adapted from figure 2.3 in [20].

[3] All charge states for impurities are modeled in the framework.

Before entering the particle loop, the time-integrated particle physics includes gas puffing, recombination and recycling (reflection) [4], which is calculated per fluid time step ($\Delta t_{fluid} = 2.2786\ \mu s$ for the simulation shown in this thesis). In the particle loop, the atomic physics, including ionization, CX and line radiation [5], is calculated per particle time step ($\Delta t_{particle} = 20$ ns), and each particle's position and velocity are updated with the same time resolution. After the particle loop, the feedback is integrated and projected back to the background plasma, such as the density source from ionization and power loss from the atomic physics.

Within one $\Delta t_{particle}$, small-angle Coulomb collisions between impurities and the background plasma [6] are calculated with even finer time resolution ($\Delta t_{coll} = 0.4$ ns), and the neoclassical impurity transport appears as a collective effect due to such binary collisions. For the collisional operator, the velocity distribution of the background plasma is assumed to be a Maxwellian shifted by the local plasma flow [22].

To sum up, the particle framework, with the atomic physics and binary collisions, has the necessary elements to simulate the XPR and the impurity transport, and the coupling to the reduced MHD model can lead to the investigation of the MHD property and even instabilities in the XPR regime. However, the following elements are currently not included: neutral-neutral collisions, molecular physics and pumping as a loss mechanism for the gasses (check figure 3 in [6]). Also, in the MHD model, $T_i = T_e$ is assumed in this thesis, which is not always sufficient for pedestal or SOL studies [25]. Therefore, the particle framework can still be expanded to include these mechanisms and coupling to the two temperature models.

[4] Recycling refers to the plasma interacting with the boundary and returning to the computational domain as neutrals; reflection refers to neutrals reaching the boundary and getting reflected back.

[5] Line radiation due to excitation is not resolved in the code, but the effective radiated power is calculated for the given background n_e and T_e, with electrons from impurities included in n_e [21].

[6] Neutral-neutral collisions are not yet included in the model.

4 Simulation Results: Towards a Stationary XPR Solution

4.1 Simulation Setup

The simulation is set up with the magnetic equilibrium and plasma condition of AUG H-mode discharge #38773 at 3.65s. In this discharge, a varying XPR vertical position was tested. Figure 4.1 shows the discharge parameters over time. The plasma current remained constant at 0.8 MA during the plateau. The magnetic configuration was lower single-null (SN) with the toroidal field strength being 1.8 T and the ion ∇B-drift [1] pointing from the plasma core to the x-point (forward field). The power from the neutral beam injection (NBI) and electron cyclotron resonance heating (ECRH) were 7.5 MW and 2.5 MW, respectively. The deuterium gas fueling rate remained constant at 2×10^{22} e^{-}/s while the nitrogen seeding rate was feedback controlled by the preset XPR vertical position.

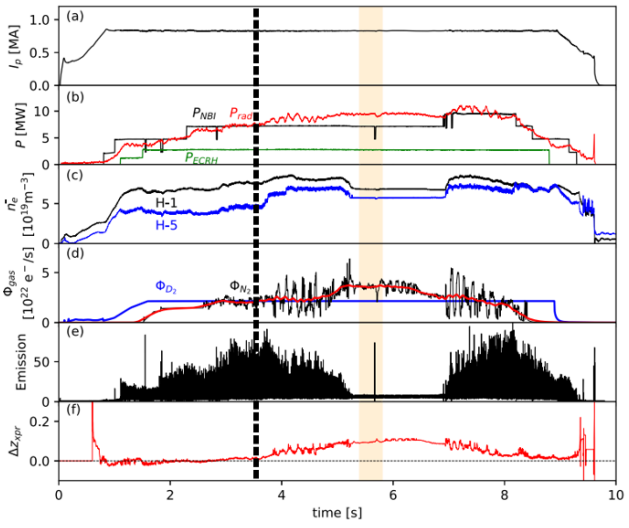

Figure 4.1: AUG discharge #38773 with 3.65 s marked by the black dashed line and the ELM suppressed regime marked in orange. The plots include the time traces of (a) plasma current (b) auxiliary heating power from NBI and ECRH and the total radiative power measured by bolometers (c) line average electron density by interferometers in plasma core (H-1) and edge (H-5) (d) deuterium gas fueling rate and nitrogen seeding rate with the smoothed data marked in red (e) emission measured by the AXUV diagnostic to show the appearance of ELMs (f) vertical distance between the radiation peak in XPR and the x-point, adapted from figure 1 in [28].

[1] Since the gradient of magnetic field strength points inboard and leads to ion drift in the direction of $B \times \vec{\nabla} B$ [39], the direction of toroidal field is often given by the ion ∇B-drift direction.

Figure 4.2 (a) shows the magnetic equilibrium that is used to generate the computational flux-aligned grid. Figure 4.2 (b) shows the safety factor q_s plotted against the poloidal magnetic flux normalized to the separatrix value (4.1), namely $\Psi_{norm} = 0$ at the magnetic axis and $\Psi_{norm} = 1$ at the separatrix.

$$\Psi_{norm} = \frac{\Psi - \Psi_{axis}}{\Psi_{sep} - \Psi_{axis}} \tag{4.1}$$

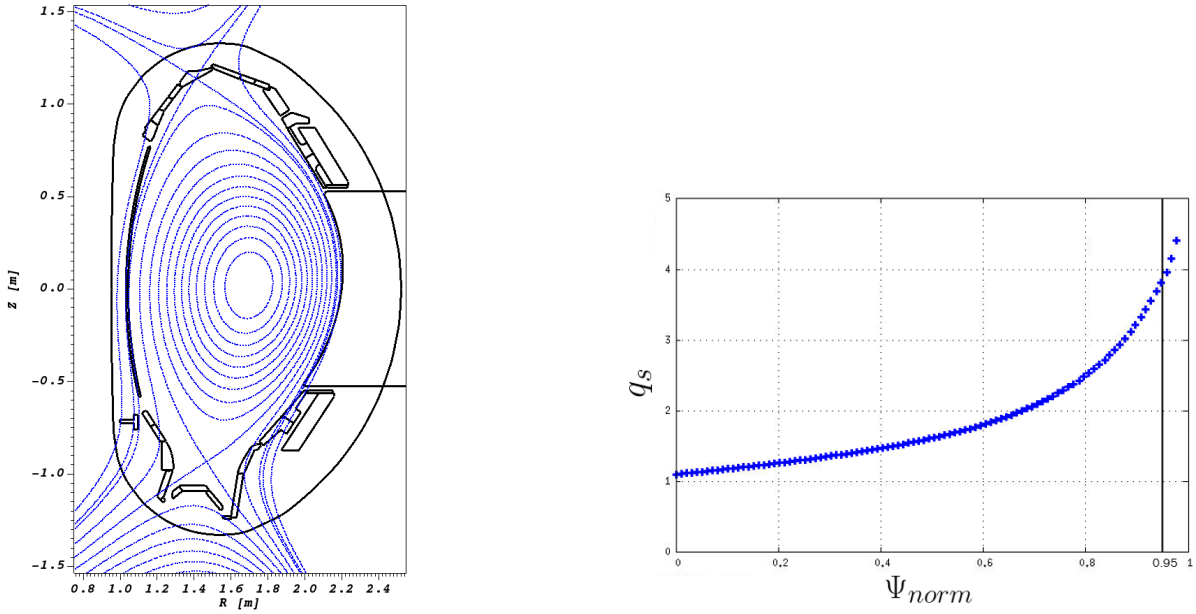

(a) (b)

Figure 4.2: (a) Magnetic equilibrium of discharge #38773 at 3.65s (b) Safety factor plotted against normalized poloidal flux with $q_{95} = 3.84$ indicated by the black line.

Figure 4.3 (a) shows the experimental measurement of outboard midplane (OMP) electron density n_e and the perpendicular particle transport coefficient $D_\perp$. On the other hand, (b) shows the OMP electron temperature T_e and the perpendicular heat transport coefficient $\chi_\perp$. Both $D_\perp$ and $\chi_\perp$ have profiles that were assumed for this study. These profiles [2] along with the magnetic equilibrium are used as inputs [3] to the simulation shown in this thesis.

However, it is important to note that the transport coefficients in JOREK are only for the background deuterium plasma. The transport of neutral particles and impurities are modeled kinetically. Also, for the simulations shown in this thesis, $D_\perp$ and $\chi_\perp$ are not chosen so that the resulting simulation has OMP profiles that match the experimental measurements. Instead, they are adjusted to maintain the OMP profiles after the effects of the kinetic neutrals and impurities. Namely, the OMP profiles remain stationary after the

[2] Note that the computation domain includes the whole main plasma and extends to the plasma facing components. The plots are done from $\Psi_{norm} = 0.8 - 1.1$ to emphasize the values near the separatrix.

[3] In JOREK, the perpendicular transport coefficients are ad hoc profiles chosen to achieve the desired plasma condition.

XPR is developed and stabilized. Currently, finding a simulation setup, with which the OMP profiles can match the experimental measurements, remains work in progress.

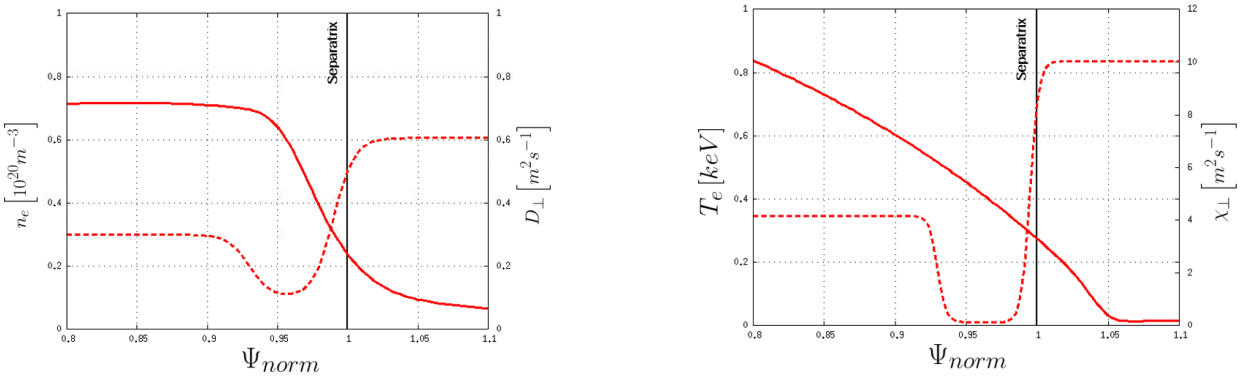

(a) (b)

Figure 4.3: From discharge #38773 at 3.65s, (a) experimental OMP electron density profile (solid) with perpendicular particle transport coefficient (dashed) (b) experimental OMP electron temperature profile (solid) with perpendicular heat transport coefficient (dashed) ($0.12\ m^2/s$ in the pedestal region).

Figure 4.4 shows the computational grid, which has higher resolution in the plasma edge, SOL and PFR, as these are the regions of particular interest in this study. Additionally, the blue boxes mark the regions in which neutral and impurity particles enter the simulation via gas puffing [4].

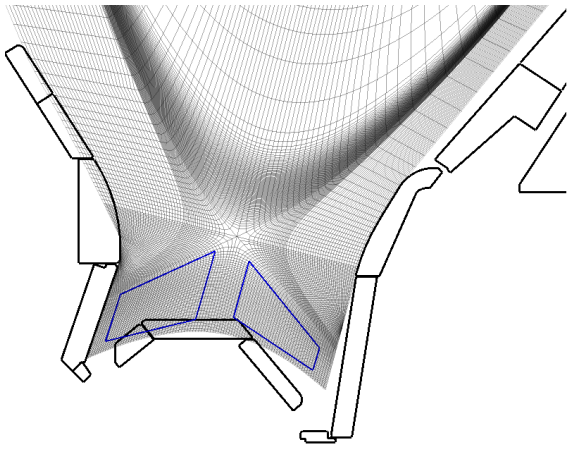

Figure 4.4: Computational flux aligned x-point grid with the regions where puffed gases enter the simulation marked by the blue boxes.

[4]The puffing locations are chosen to be in the vicinity of x-point (still entirely in the PFR) in order to speed up the effects of gas puffing on the main plasma.

4.2 Simulation procedure

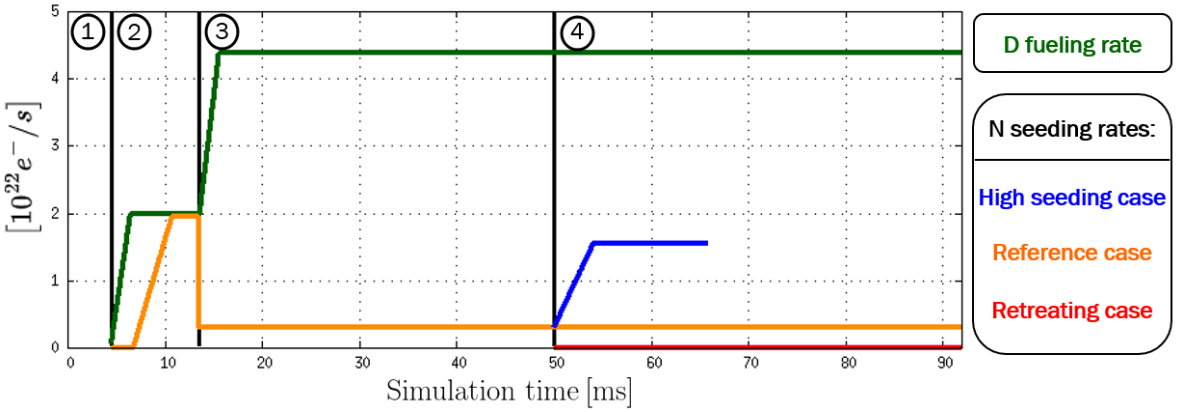

Figure 4.5: The rates of gas puffing throughout the simulations, with the D gas fueling rate (green) and N seeding rate (orange) in the reference case. In phase 4, two other cases branch out with increased (blue) or removed (red) N seeding.

The simulations shown in this thesis are done over 92 ms, and the procedure of conducting them is split into four phases. In figure 4.5, the settings for D fueling rate Γ_{D_2} and N seeding rate Γ_{N_2} are plotted. Throughout the simulation, the total heating power is kept constant at 10 MW in the plasma core. The main parameter changes and the observed physical phenomena for each phase are listed below:

- Phase 1 (deuterium plasma only): Only the base reduced model of JOREK is used, and a fluid particle source is used to maintain the density profile of the main plasma.

- Phase 2 (gas puffing ramp-up): The kinetic particle module is introduced. The fluid particle source is turned off, and kinetic neutral D particles start to be puffed, with Γ_{D_2} building up linearly until 2×10^{22} e^-/s within 2 ms. Afterwards, N seeding is initiated, with Γ_{N_2} reaching 2×10^{22} e^-/s within 4 ms. The recycling coefficients for D and N particles are 100 % and 98 %, respectively. In this phase, initially the kinetic neutrals lead to the high-field-side high-density (HFSHD) front formation. As Γ_{N_2} reaches its maximum, the impurities lead to complete detachment and XPR formation. Also, with XPR formation, the high density front leaves the HFS SOL and moves into the confined region. Discussions on HFSHD, detachment and XPR formation are in section 4.3, section 4.4 and section 4.5, respectively.

- Phase 3 (stationary XPR): In this phase, the XPR solution is stabilized and kept quasi-stationary by maintaining the D and N content. To achieve this, the recycling coefficient for D particles is reduced to 98 %, and Γ_{D_2} is increased to 4.4×10^{22} e^-/s. On the other hand, Γ_{N_2} is reduced to 3.08×10^{21} e^-/s. Discussion on the quasi-stationary XPR solution is in section 4.5.

- Phase 4 (XPR control): In this phase, the simulation branches out into three cases, which only differ

by the values of Γ_{N_2}. In the reference case, Γ_{N_2} is kept constant at 3.08 $\times$ 10^{21} e^-/s, and the XPR remains quasi-stationary. In the high seeding case where Γ_{N_2} is increased to 1.54 $\times$ 10^{22} e^-/s, the XPR develops further into the plasma core vertically, and the cold XPR core eventually develops into a MARFE [5]. In the retreating case where N seeding is turned off, it is observed that the XPR moves vertically downward and is gradually lost. Discussion of the high seeding and retreating cases, in comparison to the reference case, is shown in chapter 5.

4.3 HFSHD Formation & Loss

As mentioned in section 2.1.1 and section 2.1.2, the HFSHD front is expected to form as the kinetic neutrals are introduced, and it should disappear as both divertor targets become completely detached. The HFSHD locates in the SOL, both upstream at the IMP and downstream near the inner target (IT). Therefore, in this section, the electron density n_e is examined [6] at five time points during phase 2 and 3 of figure 4.5, showing the transition from the formation to the loss of the HFSHD region.

At the upstream, figure 4.6 shows the n_e profile on the IMP and OMP. At 8 ms, the ramp-up of D gas fueling leads to a peaking in the HFS SOL, which is not present in the LFS SOL. This indicates the formation of the HFSHD. At 11 ms, as N seeding is also ramped up, the high density in the HFS SOL broadens. At 14 ms, the HFSHD disappears, corresponding to when the divertor targets are detached and the XPR is forming. At 17 ms, the XPR is well developed, and n_e starts to peak again, but now inside the confined region. Such peaking is also present on the OMP.

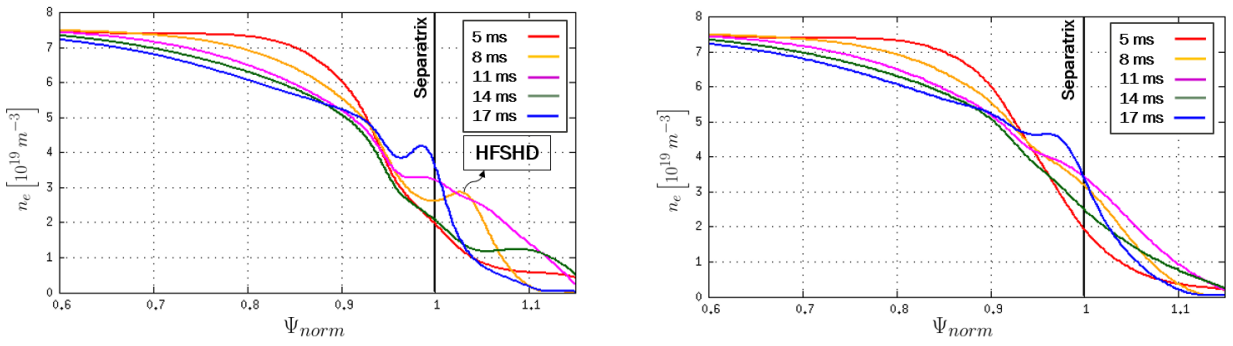

(a) (b)

Figure 4.6: Simulation results of (a) IMP (b) OMP electron density at various time points during phase 2 and the start of phase 3. The time points within the simulation phases refer to figure 4.5.

At the downstream, figure 4.7 shows the 2D plots of n_e at the same time points. At 8 ms, the high density forms at the IT, with a strong asymmetry between the HFS and LFS. The asymmetry is due to the $E \times B$

[5] The high puffing case currently cannot be run further than $\sim$ 67 ms due to numerical problems with very low temperature in the XPR core.

[6] The electron density shown in this thesis includes the contribution from both the background D plasma and impurities.

being in the opposite directions at the targets [21]. In figure 4.8, the $E \times B$ drift velocity $\vec{v}_{E\times B}$ in the poloidal direction is plotted at 8 ms. It is indicated that ionized particles from the OT drift downwards and then towards the IT in the PFR. At the IT, the high density extends upwards in the drift direction, leading to the previously shown density peaking upstream on the IMP.

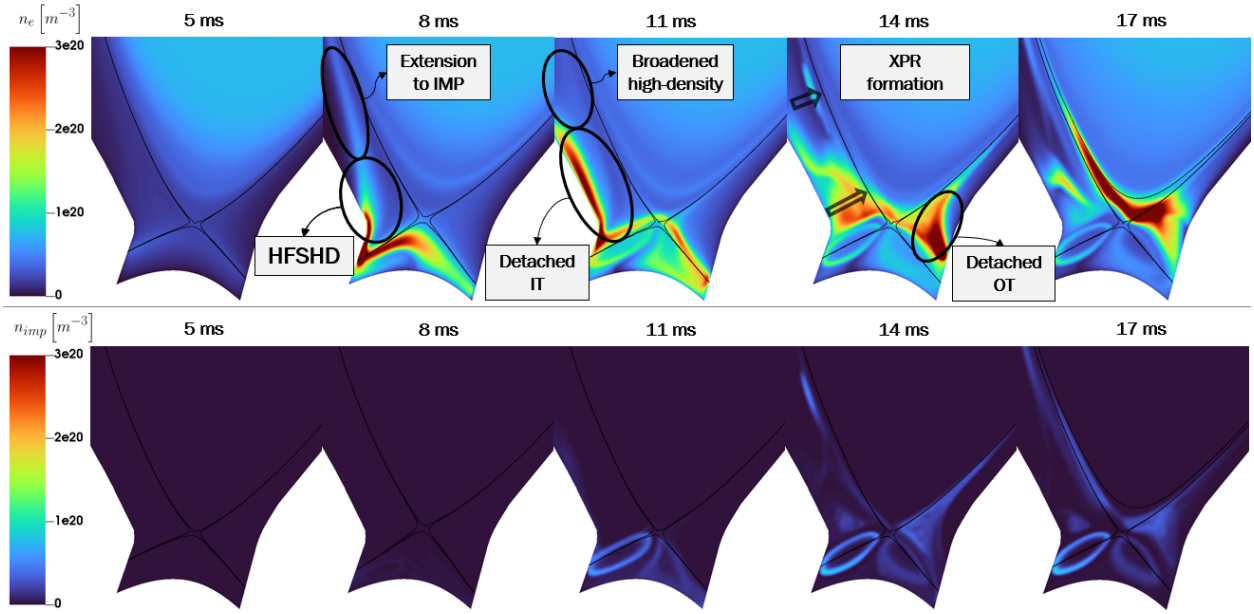

Figure 4.7: 2D plots of (a) electron density and (b) impurity number density at the same given time points as in figure 4.6.

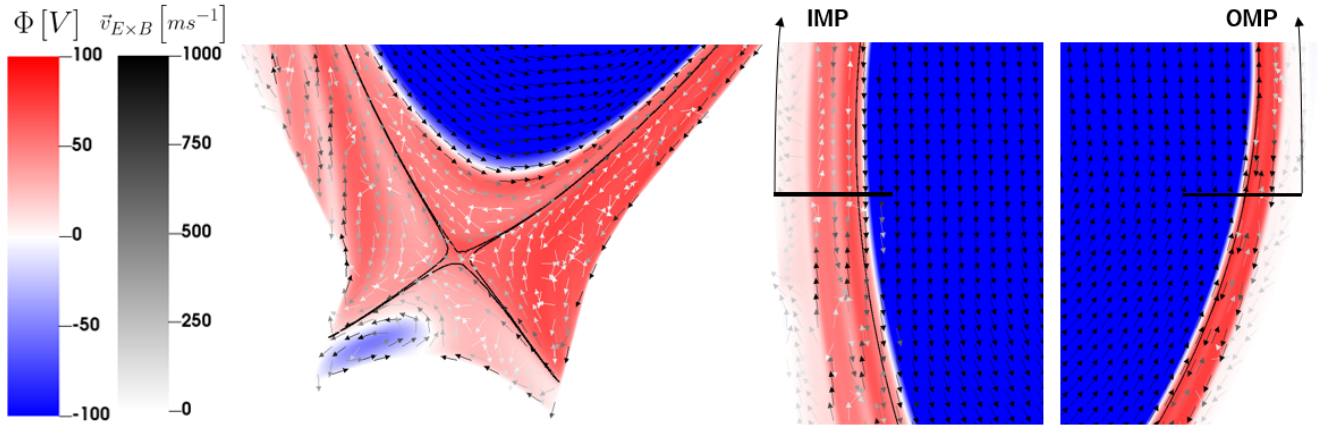

Figure 4.8: 2D plots of electric potential with poloidal $E \times B$ drift velocity at 8 ms. The magnitude of the $E \times B$ velocity is indicated by the color intensity of the vectors.

At 11 ms, n_e starts to increase along the IT as the IT starts to detach, corresponding to the onset state of detachment. At 14 ms, the HFSHD is reduced both upstream and downstream as the OT starts to detach, and the XPR starts to form as density increases slightly above the x-point, corresponding to the fluctuating state. At 17 ms, the high density moves into the confined region as the XPR is well formed, and both targets

are completely detached, corresponding to the complete detachment state. These three time points resemble the three detachment states in a forward field configuration, discussed in [30]. Further discussions on the completely detached state and the XPR are in section 4.4 and section 4.5, respectively.

4.4 Complete Detachment

The asymmetry of the $E \times B$ drift also leads to the divertor targets detach at different time point. In this section, detachment is indicated by the flattening of the total heat flux q_{tot} onto the divertor targets. In figure 4.9 (a), q_{tot} onto the simulation boundary is plotted, and the plot includes the IT, the dome and the OT. At 11 ms, as the N seeding rate reaches its maximum and the impurities start to strongly radiate away the heat flux from the upstream, the IT gets detached first, and q_{tot} is strongly flattened. The same happens to the OT at 14 ms, meaning a complete detachment while the XPR is forming. Additionally, in figure 4.9 (b), the electron temperature T_e is plotted at 17 ms, after the development of XPR, and it is clear that the entire region near the targets is below 1 eV. This shows that the XPR is inherently a detached regime.

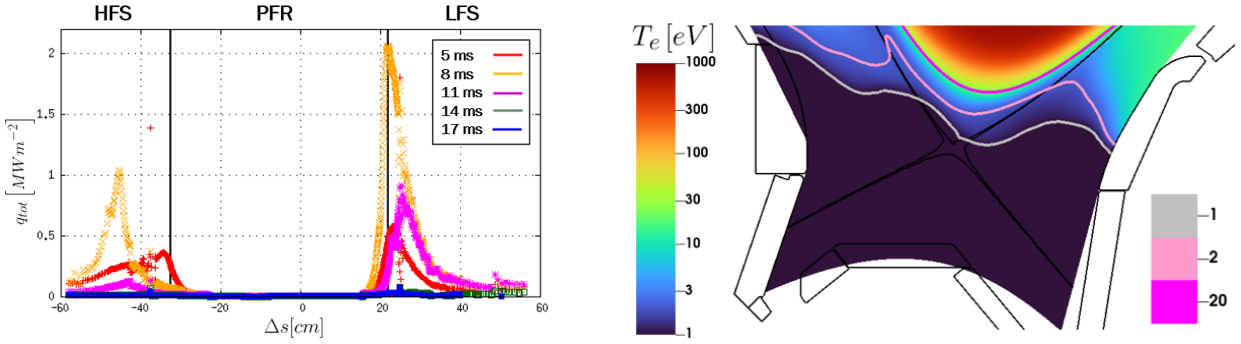

(a) (b)

Figure 4.9: (a) Total heat flux along the computation boundary from the IT to the OT at the same given time points as in figure 4.6 and (b) 2D plot of electron temperature at 17 ms with the contours of 1 (grey), 2 (pink) and 20 (magenta) eV.

4.5 XPR formation & Quasi-stationary XPR solution

In figure 4.10 (a), the total heating power P_{heat}, impurity line radiation $P_{rad,tot}$, charge exchange P_{cx} and ionization P_{ion} power loss are plotted for the reference case ($\Gamma_{N_2} = 3.08 \times 10^{21}$ e$^-$/s in phase 3 and 4). Before introducing N seeding, charge exchange and ionization from the D neutrals are the two main power losses. After N seeding reaches its maximum and the XPR starts to form, $P_{rad,tot}$ quickly increases to $\approx$ 4 MW while P_{cx} and P_{ion} reduce to $<$ 1 MW. By the end of phase 3 (50 ms), the radiative power fraction $f_{rad} = P_{rad,tot}/P_{heat}$ reaches 51 % [7], and the poloidal cross section of the impurity radiation power density

[7] Since the simulation time scale is shorter than the AUG energy confinement time scale, P_{heat} needs time to reach the edge from the core. Therefore, a more accurate measure on f_{rad} would be to calculate $P_{rad,tot}/P_{edge}$ instead, where P_{edge} is the power flux into the edge region of interest.

P_{rad} shows an upper bound at 8.5 cm above the x-point ($\Psi_{norm} = 0.985$), as shown in figure 4.10 (b). In phase 4, as Γ_{N_2} is unchanged, the XPR in the reference case remains quasi-stationary [8], with the vertical position unchanged and $P_{rad,tot}$ only marginally increased to 52 % since the D and N contents do slowly increase over time.

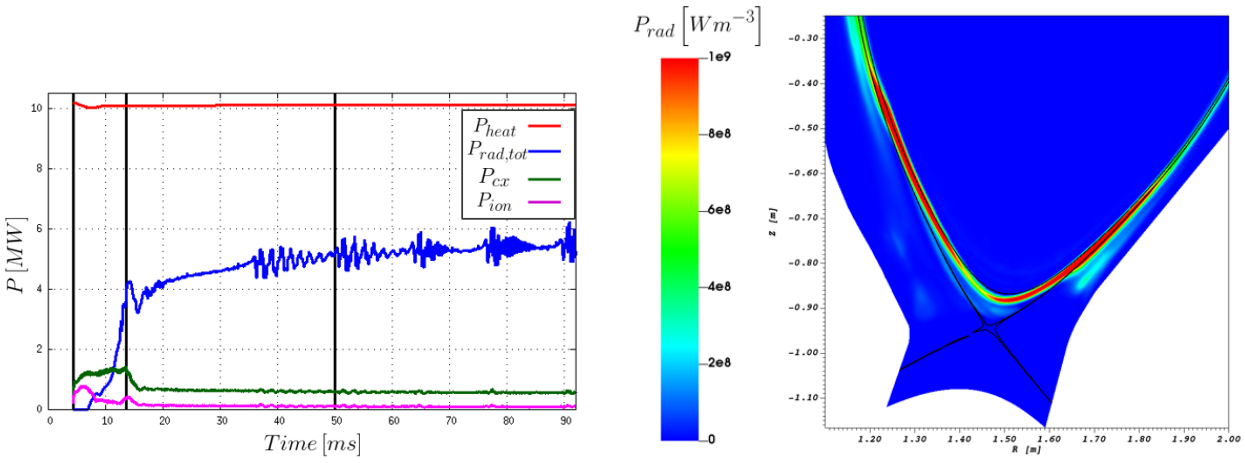

(a) (b)

Figure 4.10: (a) Time evolution of total heating power, impurity line radiation, charge exchange and ionization power loss (b) 2D plot of impurity line radiation at 50 ms, with $\Psi_{norm} = 0.985$ marked as the upper bound of the XPR. For all following plots, $\Psi_{norm} = 0.985$ is used as a reference of the vertical position above the x-point.

From figure 4.10 (b), P_{rad} appears to extend poloidally towards the midplanes. However, the XPR is experimentally observed as being poloidally localized, as shown previously in figure 2.4 [31]. It is speculated that MHD activities can prevent the impurities from reaching so far upstream, but including the MHD activities requires running 3D simulations, which is beyond the scope of this thesis. Therefore, the study of whether MHD activities result in a poloidally localized XPR solution remains a subject of future work.

In the following sections, the quasi-stationary solution is further examined at 50 ms. Firstly, several number densities (electron n_e, D neutrals $n_{D,neutral}$, D ions $n_{D,ion}$ and impurities n_{imp}) are plotted in figure 4.11, from which the impurity fraction c_{imp} and Z_{eff} are calculated and plotted in figure 4.12 (c) and (d). In figure 4.12 (a), the electron temperature T_e is used to show the location of the cold XPR core, as nitrogen starts to strongly radiate when T_e reaches 20 eV. In figure 4.12 (b), the electric potential Φ is used to show the $E \times B$ transport for the impurities, and a strong transport towards the IMP is observed, similar to the SOLPS-ITER simulation shown in figure 2.6 [28]. Additionally, the D ionization and volumetric recombination rates

[8] In figure 4.10 (a), $P_{rad,tot}$ appears to behave in a cycle of strong oscillation and stabalization in figure 4.10 (a). This is due to a simulation setting against numerical problems. The strongly radiative XPR core can sometimes reach low enough local temperature ($T_e < 0.5$ eV in this simulation) to trigger an large increase on the local $\chi_\perp$, a mechanism in JOREK to prevent the local temperature from becoming negative and causing numerical problems. Such sudden change in $\chi_\perp$ then causes solution to oscillate.

are plotted in figure 4.13, showing that the ionization front locates at the upper bound of the XPR whilst recombination occurs in the XPR core. Lastly, the XPR access parameter X_A, T_e, P_{rad} and n_{imp} are plotted along the vertical distance above the x-point to examine the criteria of XPR formation.

4.5.1 Physical Properties of the Quasi-stationary XPR solution

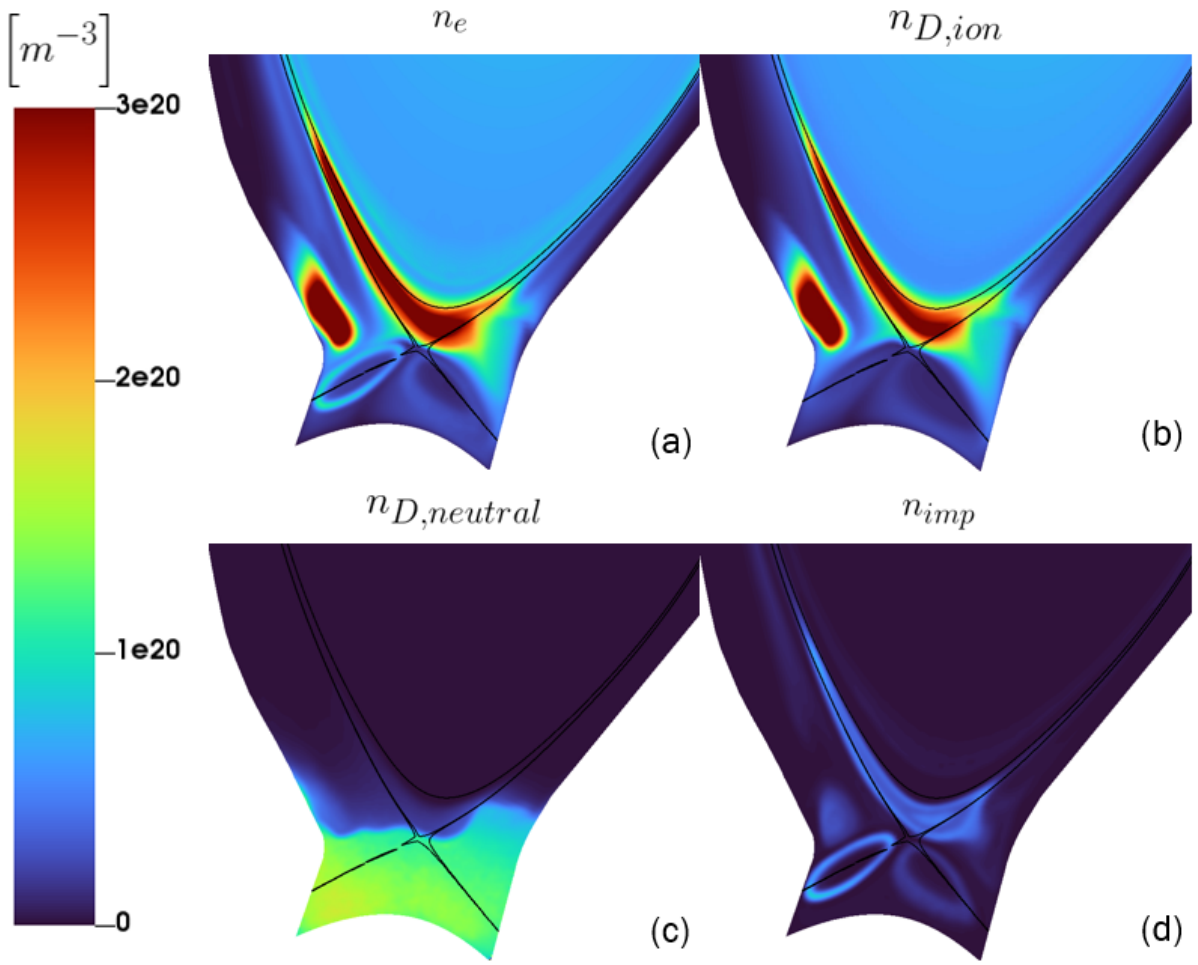

Figure 4.11: 2D plots of (a) the total electron density, (b) the D ion density, (c) the D neutral density and (d) the impurity number density at 50 ms.

Figure 4.11 shows that downstream in the XPR core, between separatrix and $\Psi_{norm} = 0.985$, the plasma is very dense. Locally, the total electron density $n_e \approx 3 \times 10^{20}$ m^3 is four times the value as in the plasma core. On the other hand, the D neutral density $n_{D,neutral}$ and the impurity number density n_{imp} are both of the order of magnitude of 10^{19} m^3 in the XPR core.

Figure 4.12 (a) shows that the XPR core is very cold, with T_e reduces to between 1 eV and 2 eV [9]. Due to the low temperature in the XPR volume, neutrals can travel kinetically into the confined region and remain

[9] For numerical reasons, impurities radiation, charge exchange and ionization are turned off at T_e <1 eV. Recombination is turned off at $T_e < 0.2$ eV.

in the XPR core before getting ionized at its upper bound. Additionally, the contour of $T_e = 20$ eV appears to match the flux surface $\Psi_{norm} = 0.985$ very well, which is also the upper bound of the strongly radiative region from figure 4.10 (b). Therefore, the contour of $T_e = 20$ eV can be used to approximate the edge of the XPR.

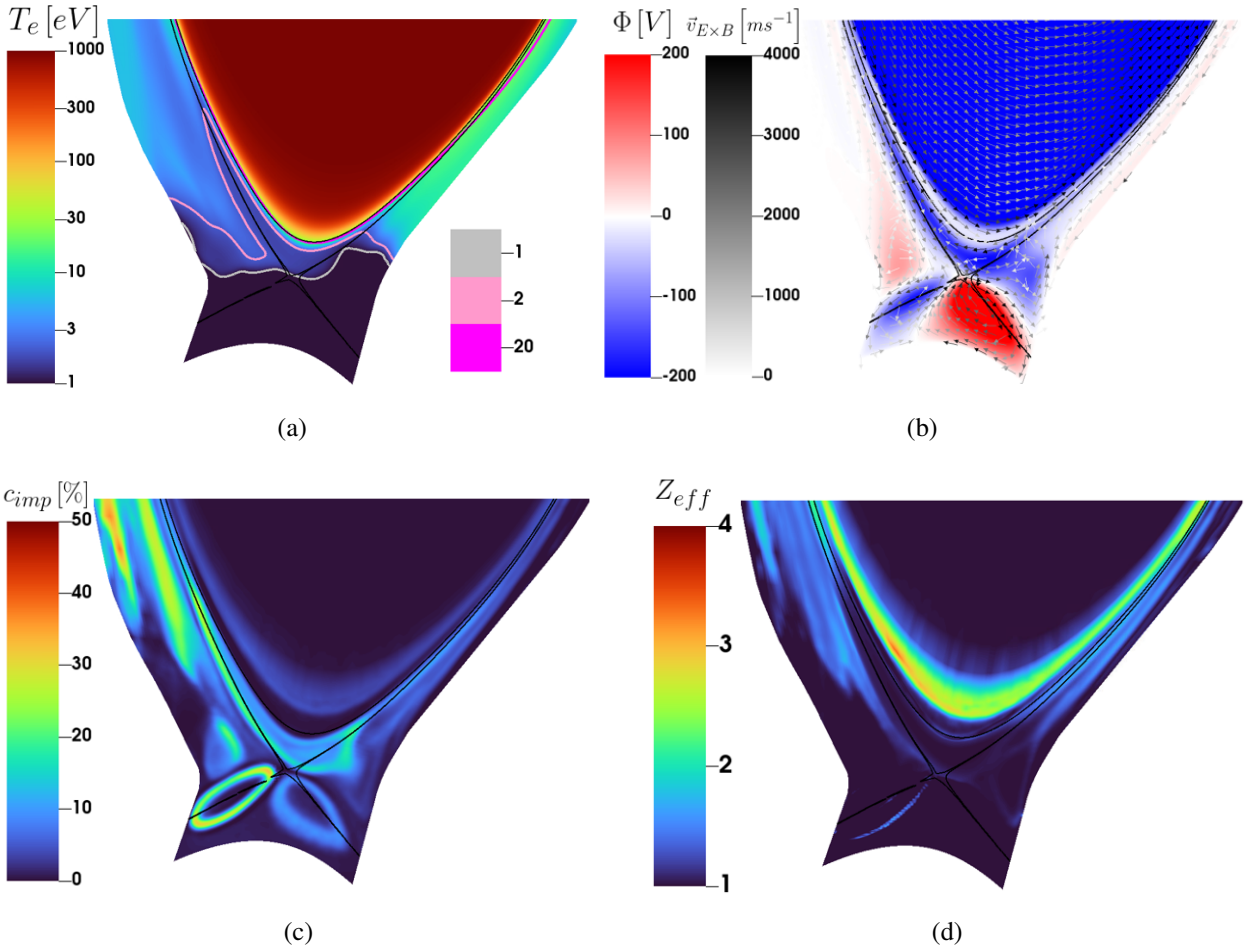

Figure 4.12: 2D plots of (a) electron temperature with the contours of 1 (grey), 2 (pink) and 20 (magenta) eV, (b) electric potential with the vectors indicating the poloidal $E \times B$ drift velocity, (c) Impurity fraction and (d) Z_{eff} at 50 ms.

The high densities of D ions and impurities tend to extend towards the IMP. This is due to the $E \times B$ transport [10]. In figure 4.12 (b), the electric potential Φ is plotted along with the $E \times B$ drift velocity $\vec{v}_{E\times B}$, and a strong poloidal drift from the XPR core towards the IMP is present. This drift results from a potential well in the XPR core and a thin potential hill above the XPR. This drift is similar to what is observed in the SOLPS simulation result shown by figure 2.6 [28].

In figure 4.12 (c) and (d), the impurity fraction is calculated as $c_{imp} = n_{imp}/n_e$ and the Z_{eff} is calculated

[10] In the simulations shown in this thesis, the $E \times B$ transport serves as the only cross-field transport mechanism for the impurities with any charge state. The neoclassical impurity transport mentioned in section 3.2 is not yet turned on for this simulation setting, and the inclusion of it remains in the work in progress.

as equation (4.2), where <Z_{imp}> is the locally average charge state of the impurities. These plots show that c_{imp} saturates at $\approx 15\ \%$ in the XPR core, and Z_{eff} remains ≈ 1 as the local temperature is not high enough to raise the charge state of the impurities. Instead, Z_{eff} is higher in the region above the XPR.

$$Z_{eff} = \frac{n_{D,ion} + n_{imp} < Z_{imp} >^2}{n_{D,ion} + n_{imp} < Z_{imp} >} = \frac{n_{D,ion} + n_{imp} < Z_{imp} >^2}{n_e} \tag{4.2}$$

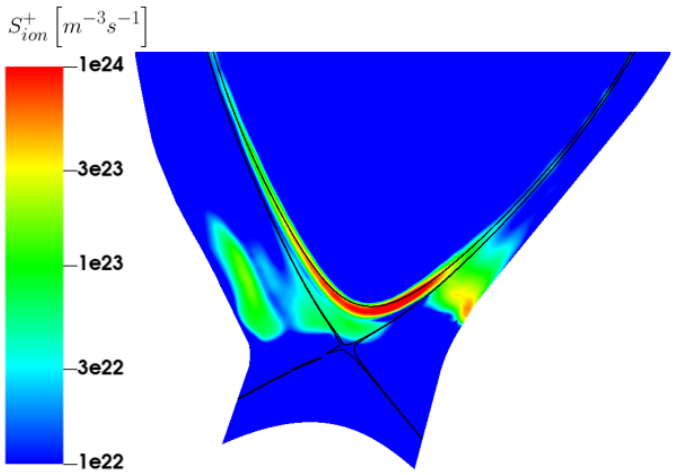

(a)

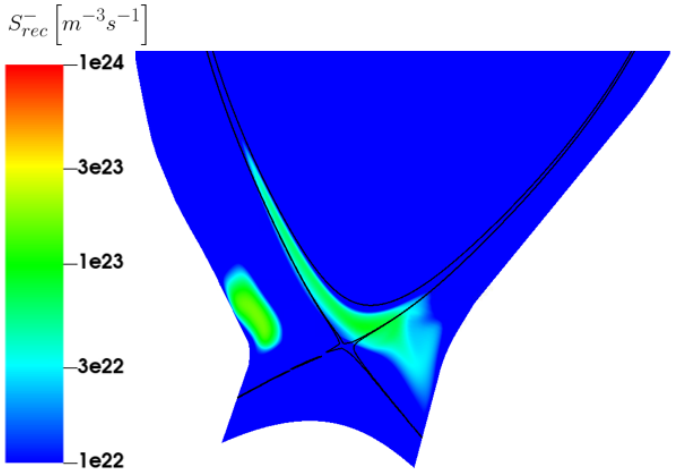

(b)

Figure 4.13: 2D plots of deuterium ion (a) source from ionization and (b) sink from recombination at 50 ms.

Figure 4.13 (a) shows the rate of D ionization S^+_{ion}, which indicates that the ionization front locates at the upper bound of the XPR. The ionization power loss then helps to reduce T_e to $\approx$ 20 eV, where impurity radiation starts to take over. Figure 4.13 (b) shows the rate of D volumetric recombination, which is high in the XPR core, where T_e is below 2 eV and $n_{D,ion}$ is high.

To sum up, at the upper bound of the XPR, the ionization of the D neutral particles serves as an ion source for the XPR core, and the ionization power loss is responsible for reducing T_e to 20 eV, low enough for

impurity line radiation to take over. On the other hand, in the XPR core, impurity radiation is responsible for further reducing T_e to ≈ 1 eV, and recombination occurs as a sink of D ions.

4.5.2 Analysis on Access Parameter through the XPR Core

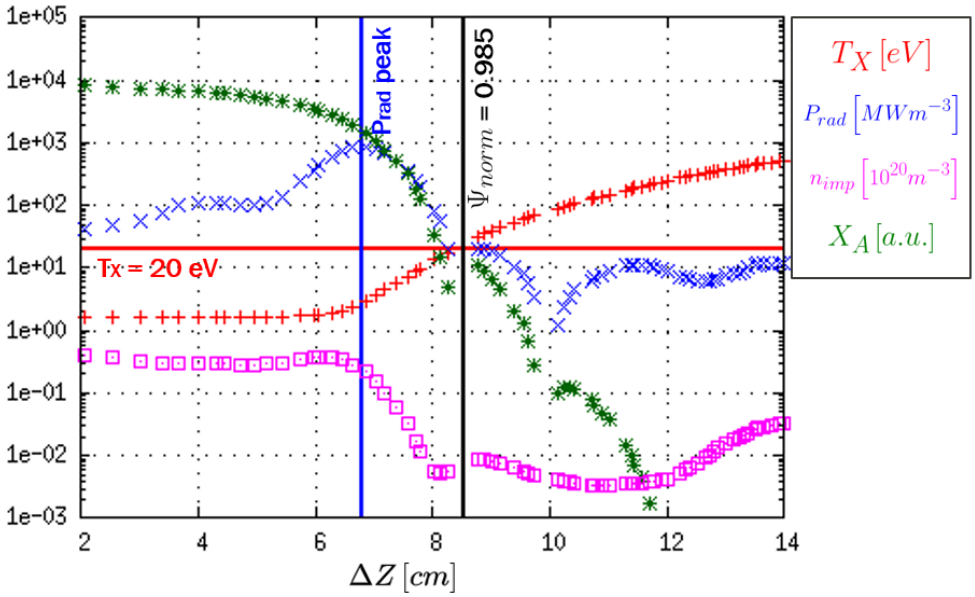

Figure 4.14: Downstream parameters plotted against vertical position above the x-point: (red) electron temperature, (blue) impurity line radiation, (magenta) impurity number density and (green) XPR access parameter at 50 ms. The black vertical line indicates the flux surface $\Psi_{norm} = 0.985$. The blue vertical line indicates the peak of P_{rad}. The red horizontal line indicates $T_X = 20$ eV.

This section includes a discussion on the criteria for XPR formation. In figure 4.14, the downstream electron temperature T_X, impurity line radiation P_{rad}, impurity number density n_{imp} and the calculated XPR access parameter X_A are plotted from $\Delta Z = 2 \sim 14$ cm above the x-point. In this plot, the edge of the XPR ($\Psi_{norm} = 0.985$) is marked at $\Delta Z = 8.5$ cm, which coincides nicely with where $T_X = 20$ eV, same as previously shown in figure 4.12 (a). Below $\Delta Z = 8.5$ cm, P_{rad} rapidly increases and peaks at $\Delta Z = 6.8$ cm, indicating the location of the XPR core. As P_{rad} increases from the edge to the core of the XPR, the following three conditions are observed:

- T_X gets below 20 eV for the impurities to start to strongly radiate.
- n_{imp} increases towards the XPR core.
- X_A also increases rapidly towards the XPR core, meaning the D neutral particles [11] can travel from the PFR into the XPR core without being ionized since the ionization front is at the upper edge of the XPR, as shown in figure 4.13 (a).

In chapter 5, the same vertical profile analysis is used to help understand the mechanism behind a strongly

[11] $X_A \propto n_{D,neutral}$ from equation (2.11).

developing XPR and a retreating XPR. By comparing these two cases with the reference case, the aim is to find out the direct and indirect effects from the nitrogen seeding to the XPR solution.

5 Other XPR Simulation: Control and Stability

In this chapter, the two alternative XPR simulations in phase 4 are analyzed. The nitrogen seeding rates Γ_{N_2} in the two cases comparing to the reference case are indicated in figure 5.1. The high seeding case, where Γ_{N_2} is further increased to 1.54×10^{22} e^-/s, shows an upward vertical movement of the XPR and eventually characteristics of a MARFE towards the end of the simulation. The retreating case, where nitrogen seeding gets completely turned off and the nitrogen content in the computational domain gradually decreases, shows an downward movement and eventually the loss of the XPR.

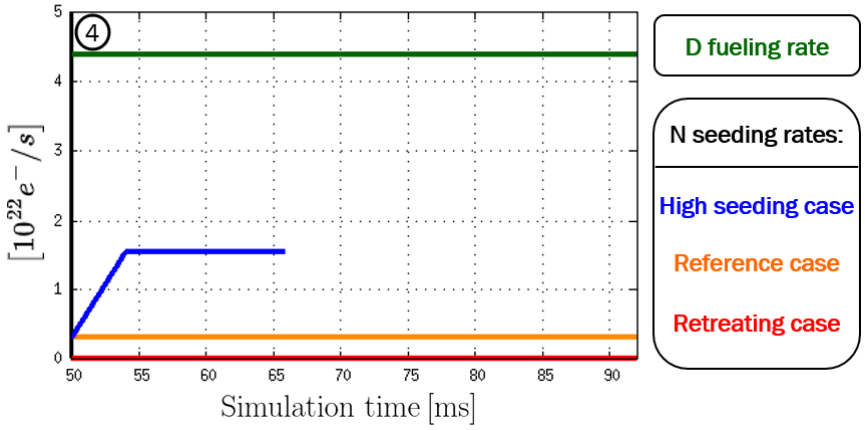

Figure 5.1: Time evolution of deuterium fueling rate (green) and nitrogen seeding rate in the high seeding case (blue), the reference case (orange) and the retreating case (red).

5.1 The High Seeding Case

In figure 5.2, $P_{rad,tot}$, P_{cx} and P_{ion} are plotted over time in the high seeding case before the simulation ends due to numerical issues, with the four vertical lines indicating the four time points chosen to study the development of the XPR:

- 50.2 ms serves as a reference.
- At 57.9 ms, the XPR starts to develop vertically upwards.
- At 61.4 ms, the total radiative fraction f_{rad} reaches 60 %. Temperature in the XPR core starts to further decrease and volumetric recombination is enhanced locally. The cold XPR core starts to develop into a MARFE.
- At 64.1 ms, a MARFE scenario is achieved.

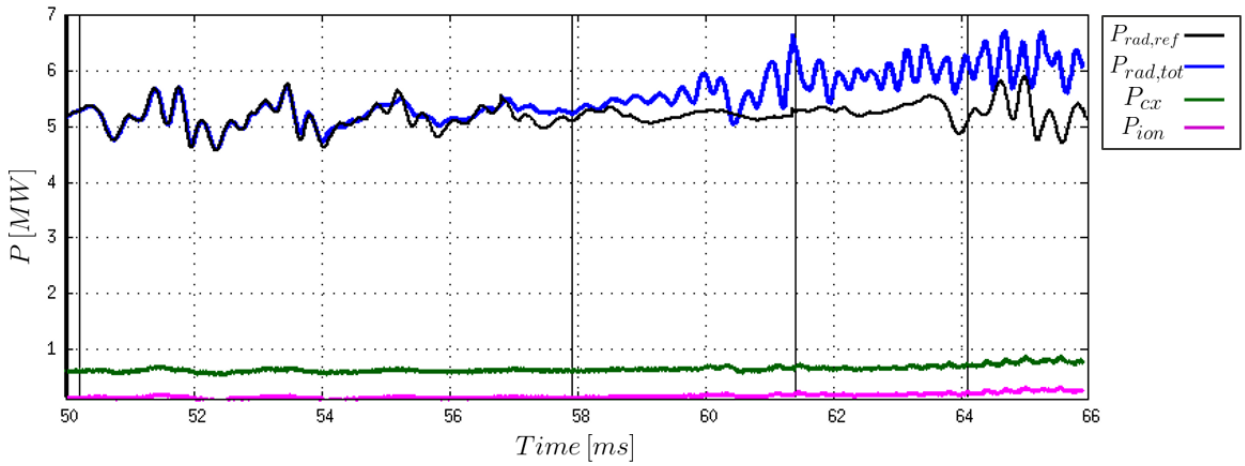

Figure 5.2: Time evolution of different power losses in the high seeding case: impurity line radiation (blue), charge exchange (green) and ionization (magenta). $P_{rad,tot}$ in the reference case is added in black for comparison. The four vertical lines indicate the time points for analysis.

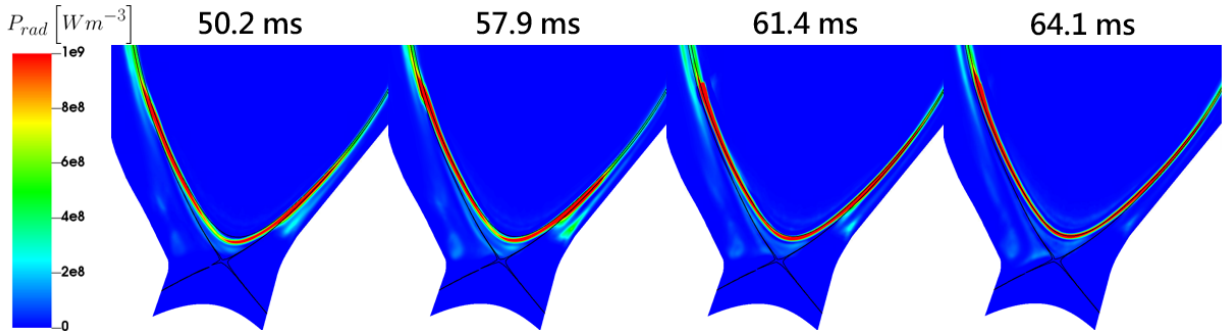

Figure 5.3: 2D plots of P_{rad} at the four time points, with the flux surface ($\Psi_{norm} = 0.984$) marked.

Figure 5.3 shows the poloidal cross section of P_{rad} at the four time points. At the downstream, the XPR develops from below the flux surface ($\Psi_{norm} = 0.984$) to slightly above it. The same development can be seen more pronounced at the upstream on the HFS. This is again due to the poloidal $E \times B$ drift that transports the impurities towards the IMP. However, it should be noted that the XPR is experimentally observed to be poloidally localized [31]. Moreover, MHD activities also play a role in the impurity transport. Therefore, the transition to 3D simulations to include MHD activities might be necessary to model the vertical development of the XPR without the strong poloidal extension. In this section, the analysis is done on the vertical profiles directly above the x-point, and the poloidal extension is not further discussed.

Figure 5.4 shows the vertical profiles of P_{rad} and T_X above the x-point plotted at the four time points mentioned above. At 50.2 ms, the profiles are identical to the reference case, with P_{rad} peaking at $\Delta Z = 6.8$ cm and $\Delta Z = 8.4$ cm indicating the upper bound ($T_X = 20$ eV) of strong impurity radiation. At 57.9 ms and 61.4 ms, it is observed that the peak of P_{rad} moves vertically upwards (to $\Delta Z = 7.4$ cm and then $\Delta Z = 8.0$ cm), and P_{rad} also peaks at higher values. Additionally, in contrast to the reference case, the

highly radiative region extends slightly beyond the vertical position of $T_X = 20$ eV, indicating that there is an increase of n_{imp} at the upper edge of the XPR [1]. At 64.1 ms, the peak of P_{rad} further develops to $\Delta Z = 8.7$ cm, and the temperature in the XPR core drastically decreases to ≈ 0.03 eV, with which a MARFE can be formed.

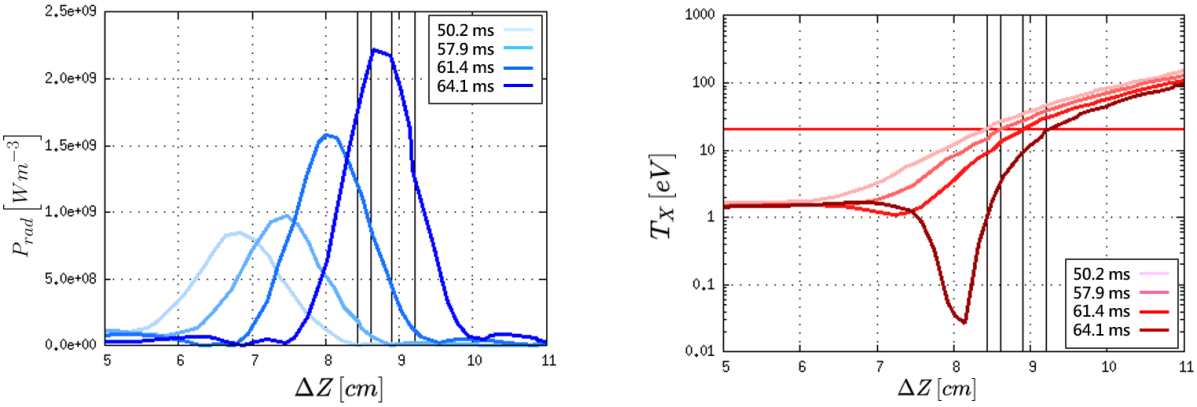

(a) (b)

Figure 5.4: Vertical profiles of (a) P_{rad} and (b) T_X above the x-point in the high seeding case, with the vertical lines marking the vertical position where $T_X = 20$ eV at the four time points.

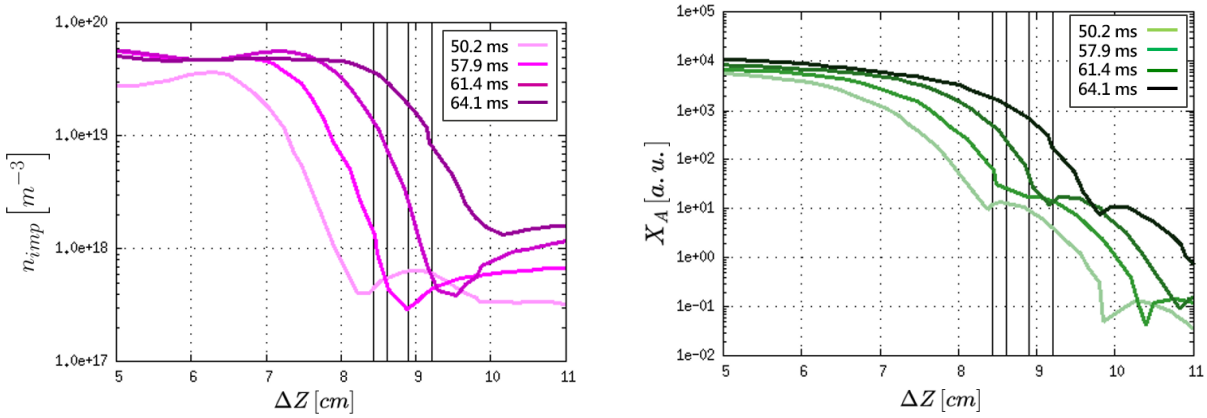

(a) (b)

Figure 5.5: Vertical profiles of (a) n_{imp} and (b) X_A above the x-point in the high seeding case at the same time points.

[1] $P_{rad} \propto c_{imp} \propto n_{imp}$ from equation (2.8).

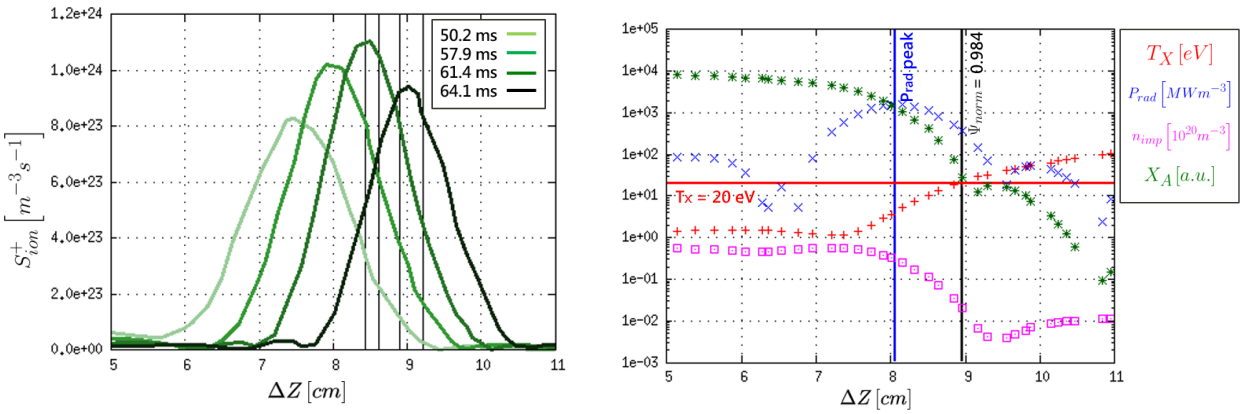

(a) (b)

Figure 5.6: Vertical profiles of (a) S^+_{ion} at the same time points and (b) T_X, P_{rad}, n_{imp} and X_A plotted together at 61.4 ms, before the MARFE formation, with the vertical position of $T_X = 20$ eV ($\Psi_{norm} = 0.984$) and the peak of P_{rad} marked in black and blue, respectively.

In figure 5.5, n_{imp} and X_A are plotted to examine the effects of impurities and deuterium neutrals on the dynamics of the XPR moving vertically upwards. Regarding n_{imp}, the impurities accumulate in the XPR core due to the increase of the seeding rate. The increase of n_{imp} then extends from the XPR core to the edge of the XPR, which leads to the increase of P_{rad} at the upper bound of the XPR, where the deuterium ionization front is located. With the highly radiative region overlapping more with the ionization front, P_{rad} takes over as the main power loss mechanism, further reducing T_X at the upper bound of the XPR. Then, as shown in figure 5.6 (a), the ionization front is pushed further into the plasma core, and the deuterium neutral particles can travel beyond the previous upper bound of the XPR until reaching the new ionization front. The increase of deuterium neutral density then leads to increasing X_A at the previous upper bound, indicating that the XPR has extended vertically upwards. In figure 5.6 (b), T_X, P_{rad}, n_{imp} and X_A are plotted together at 61.4 ms, before the XPR core drastically cools down. Comparing to the reference case from figure 4.14, the major differences are the increased P_{rad} and n_{imp} at the upper bound of the XPR. This suggests a direct relation between Γ_{N_2} and the XPR vertical position, as one expects from the experimental results [2].

To sum up, the process of a XPR moving upwards can be summarized into a sequence of the following effects:

- Increase of n_{imp} from the XPR core to the upper bound leads to an overlapping of the highly radiative region over the ionization front.
- Ionization front develops further into the plasma core, and the previous upper bound further cools down.
- D neutrals density increases at the previous upper bound, local X_A increases.
- A new XPR solution with higher vertical position of the XPR core and the upper bound is reached.

To discuss on the last time point (64.1 ms), where the XPR core drastically cools down, the vertical profiles

of the volumetric recombination rate S_{rec}^{-} and the MARFE occurrence parameter M_A are plotted in figure 5.7. Below the peak of P_{rad}, the drastic decrease of T_X leads to locally a strong peaking of S_{rec}^{-} and M_A. The increase of these two quantities indicate that the cold XPR core has developed into a MARFE.

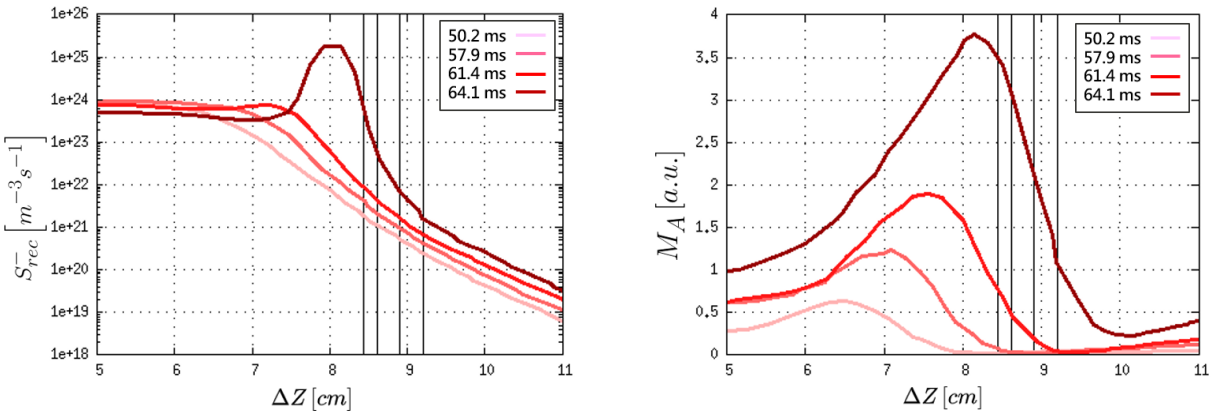

(a) (b)

Figure 5.7: Vertical profiles of (a) S_{rec}^{-} and (b) M_A at the same time points.

Additionally, figure 5.8 shows that a region with strong recombination already appears upstream on the HFS before downstream. This is due to the same poloidal $E \times B$ drifts that transports deuterium ions and impurities poloidally towards the IMP.

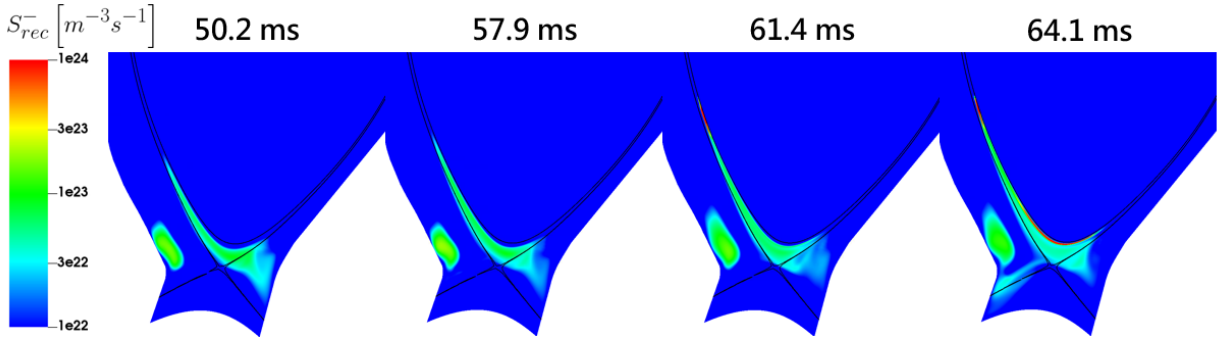

Figure 5.8: 2D plots of S_{rec}^{-} at the same time points, with the flux surface ($\Psi_{norm} = 0.984$) marked.

5.2 The Retreating Case

In figure 5.9, $P_{rad,tot}$, P_{cx} and P_{ion} are plotted over time in the retreating case, with the four vertical lines indicating the four time points chosen to study the development of the XPR:

- 50.2 ms serves as a reference.
- At 75.0 ms, the XPR starts to develop vertically downwards.
- At 83.9 ms, the XPR start to move outside of the confined region and enter the SOL.
- At 91.4 ms, the XPR is lost.

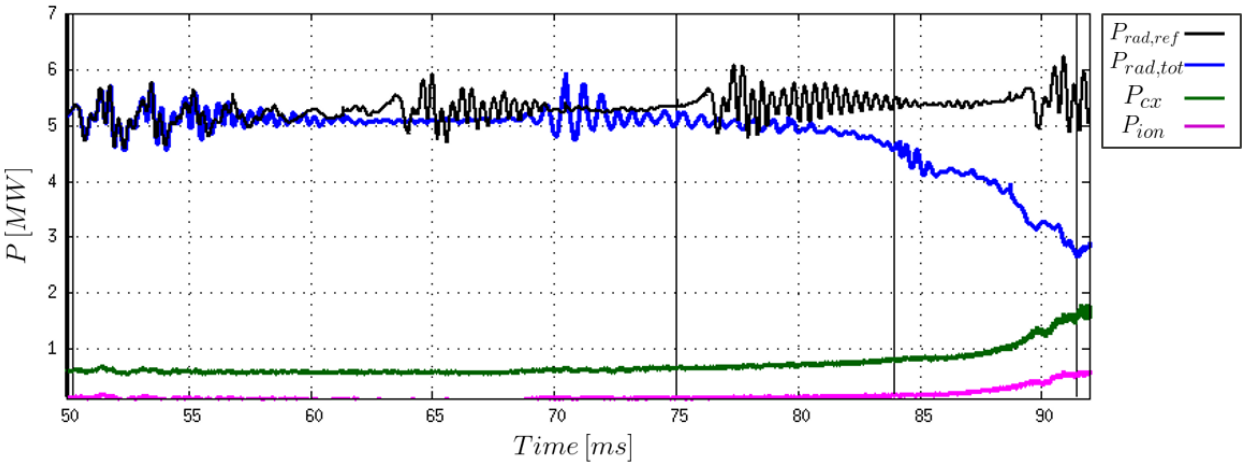

Figure 5.9: Time evolution of different power losses in the retreating case: impurity line radiation (blue), charge exchange (green) and ionization (magenta). $P_{rad,tot}$ in the reference case is added in black for comparison. The four vertical lines indicate the time points for analysis.

In figure 5.10, the vertical profiles of P_{rad} and T_X are plotted at the four time points. At 50.2 ms, the profiles are identical to the reference case, with P_{rad} peaking at $\Delta Z = 6.8$ cm and $\Delta Z = 8.4$ cm indicating the upper bound ($T_X = 20$ eV) of strong impurity radiation. At 75 ms and 83.9 ms, it is observed that the peak of P_{rad} moves vertically downwards (to $\Delta Z = 6.2$ cm and $\Delta Z = 4.9$ cm) and P_{rad} peaks at lower values. As P_{rad} gets weaker, the XPR volume starts to heat up, indicating that P_{rad} is not high enough to maintain the power balance. At 91.4 ms, P_{rad} weakly peaks at $\Delta Z = 2.6$ cm and $\Delta Z = 10.9$ cm, and T_X no longer gets lower than $T_X = 20$ eV above the x-point, indicating a loss of the XPR solution. In this section, the first three time points are used to study the dynamics of a retreating XPR. Afterwards, the transition between 83.9 ms and 91.4 ms is further analyzed to study the loss of the XPR.

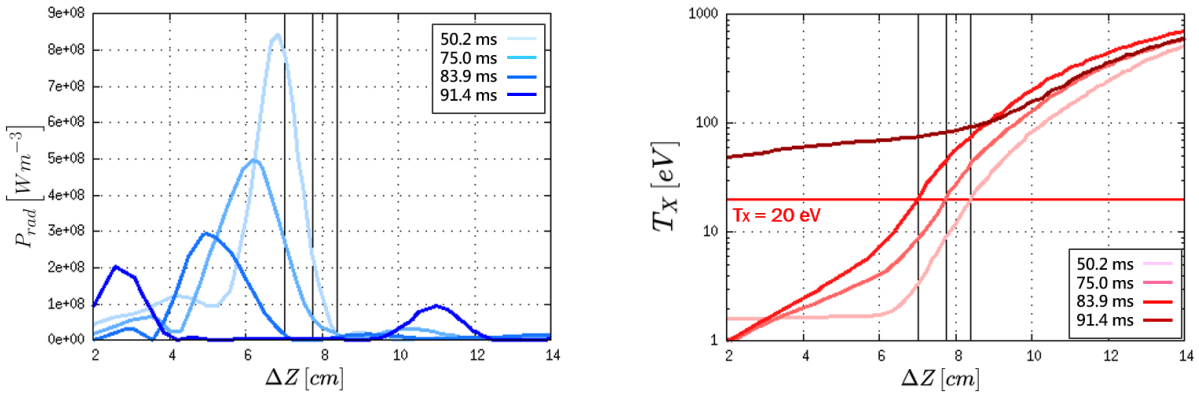

(a) (b)

Figure 5.10: Vertical profiles of (a) P_{rad} and (b) T_X in the retreating case, with the vertical lines marking the vertical position where $T_X = 20$ eV at the first three time points.

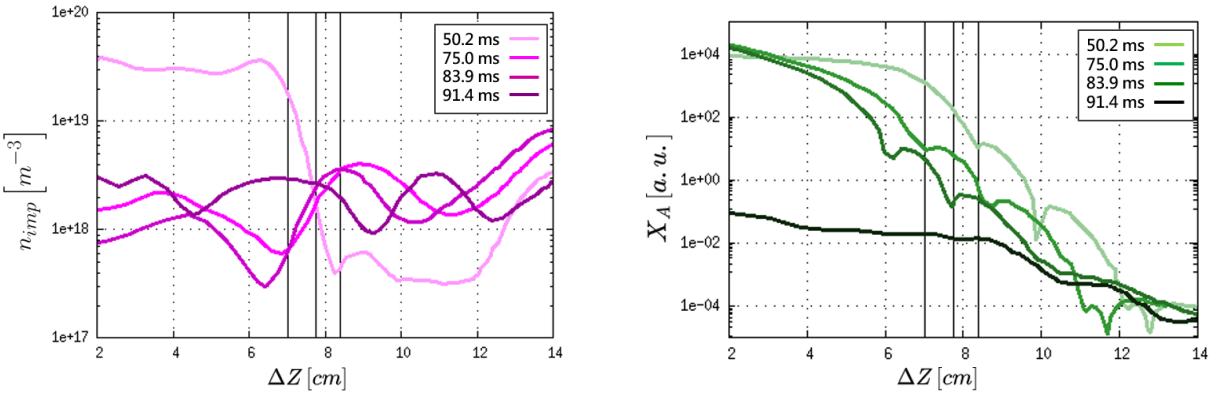

(a) (b)

Figure 5.11: Vertical profiles of (a) n_{imp} and (b) X_A in the retreating case at the same time points.

In figure 5.11, n_{imp} and X_A are plotted to examine the effects of impurities and deuterium neutrals on the dynamics of the XPR moving vertically downwards. Regarding n_{imp}, the impurities originally concentrate in the XPR core, with some particles transported further into the plasma core due to the poloidal $E \times B$ drifts from the electric potential hill above the XPR, as previously shown in figure 4.12 (b). After nitrogen seeding is turned off, n_{imp} is reduced in the XPR core by one order of magnitude, weakening P_{rad} in the power balance. This leads to X_A gradually decreasing in the XPR volume. At 91.4 ms, the XPR is lost despite n_{imp} is not further reduced above the x-point. While the XPR develops downwards, the reduction of X_A indicates a gradual depletion of D neutral particles from ionization.

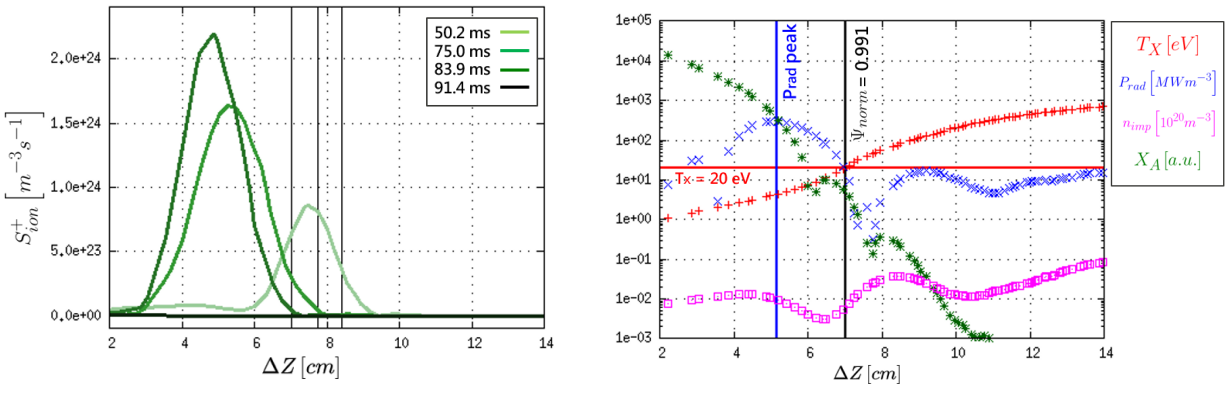

(a) (b)

Figure 5.12: Vertical profiles of (a) S^+_{ion} at the same time points and (b) T_X, P_{rad}, n_{imp} and X_A plotted together at 83.9 ms, with the upper bound of XPR ($\Psi_{norm} = 0.991$) and the peak of P_{rad} marked in black and blue, respectively.

Figure 5.12 (a) shows that as P_{rad} weakens, S^+_{ion} starts to peak in the XPR core. The power balance is then maintained by ionizing the deuterium neutrals, and the ionization front moves from the upper bound to the core of the XPR. After all the neutrals are consumed and deuterium ionization is out of the picture, the

XPR is lost. In figure 5.12 (b), T_X, P_{rad}, n_{imp} and X_A are put together at 83.9 ms, before the loss of the XPR. Comparing to the reference case from figure 4.14, the major differences are the lower values of P_{rad} and n_{imp} in the XPR core. Additionally, it is observed that X_A is reduced at the upper bound of the XPR, meaning that less neutrals can reach there and maintain neutral. Eventually, with the lack of power losses, the upper bound of the XPR starts to heat up, leading to the cold XPR core developing downwards.

To examine the process of losing the XPR, figure 5.13 shows the poloidal cross-sections of P_{rad}, n_{imp}, electric potential Φ and S_{ion}^{+} plotted at 83.9 ms, 91.4 ms and two more time points in between. The four time points show different stages of losing the XPR.

At 83.9 ms, there are two highly radiative regions. One extends poloidally towards the IMP and the other towards the OMP, with the one on the HFS extends further upstream. The two highly radiative regions also correspond to where the impurities are concentrated. Additionally, the potential well in the XPR core and the thin potential hill above the XPR are still present. The ionization front also moves into the XPR core, depleting the deuterium neutral density.

At 87.1 ms, the highly radiative region on the LFS has crossed the separatrix and entered the SOL, meaning the XPR is partially lost. With the loss of high impurity density on the LFS in the confined region, the potential well also disappears locally, leaving the potential well only present on the HFS.

At 89.6 ms, the same turn of events happens on the HFS, leaving the highly radiative and ionizing region only slightly above the x-point. This indicates that the XPR is soon to be completely lost. With the loss of high impurity density on the HFS in the confined region, the potential well is no longer present in the confined region and has moved into the HFS SOL.

At 91.4 ms, with the ionization front and the highly radiative region being completely outside the confined region, the XPR has been lost, and the impurities concentrate on the HFS, in the SOL and PFR. Additionally, n_{imp} in the confined region is not further reduced after the XPR is lost, but forming an XPR again is no longer possible because of the absence of deuterium neutrals there.

To sum up, the process of a XPR moving downwards and eventually being lost can be summarized into a sequence of the following effects:

- Reduction of n_{imp} leads to a reduction of P_{rad} in the XPR core.
- Ionization rate of deuterium neutrals increases in the XPR core to maintain the power balance.
- Less neutrals can reach the upper edge of the XPR, local X_A decreases and the XPR starts to retreat.
- Upon consuming all the neutrals in the gradually lowering XPR core, power balance cannot be maintained and the XPR is lost without further reducing the local n_{imp}.

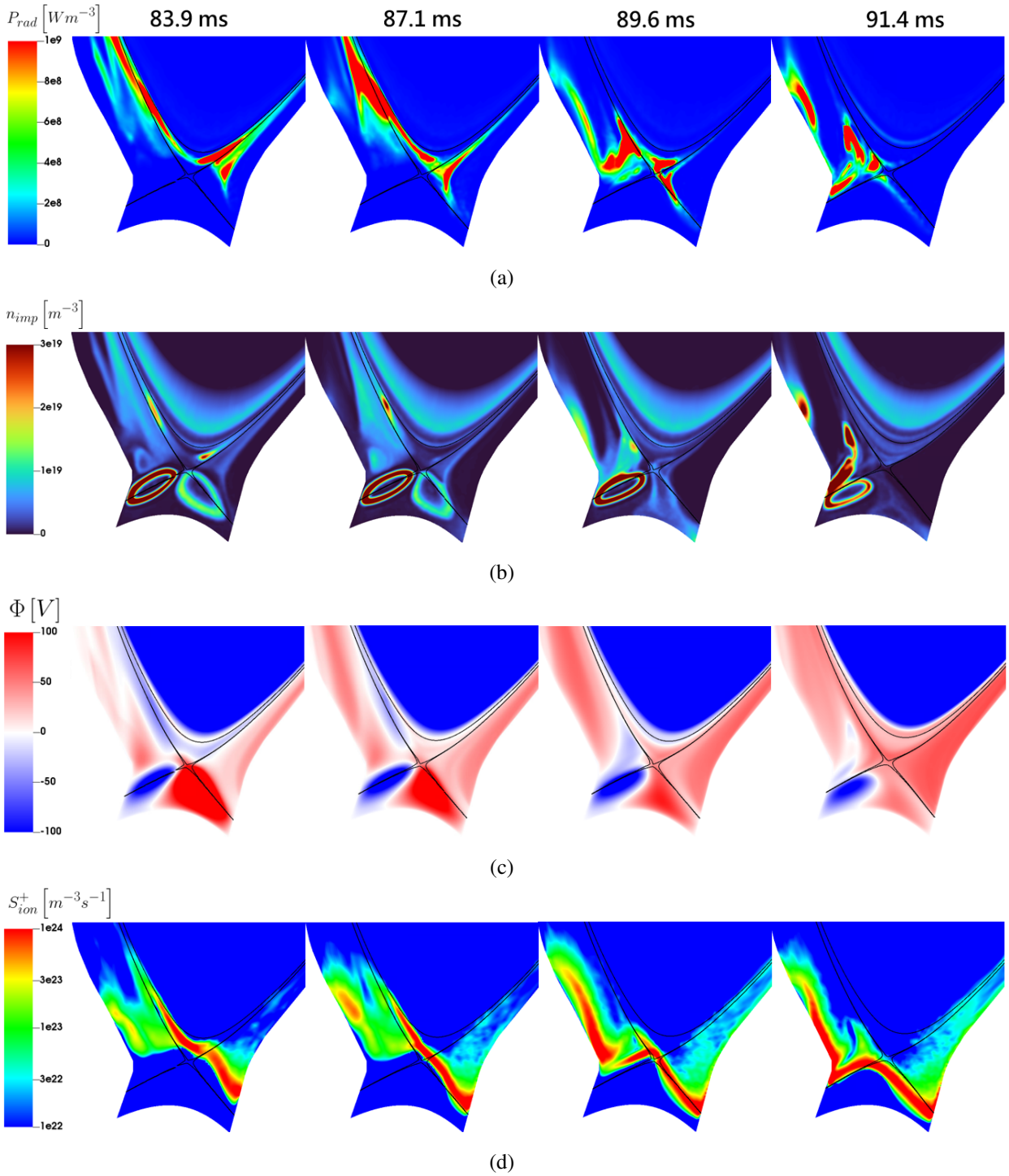

Figure 5.13: 2D plots of (a) P_{rad}, (b) n_{imp}, (c) Φ and (d) S^{+}_{ion} at four time points between before (83.9 ms) and after (91.4 ms) the loss of the XPR, with the flux surface ($\Psi_{norm} = 0.991$) marked as the upper bound of the XPR at 83.9 ms.

6 Conclusion & Outlook

This thesis aimed to investigate the formation and properties of the X-point radiator (XPR) as a potential solution to the power exhaust problem in future tokamak reactors [2]. Throughout the thesis project, axisymmetric (2D) simulations were conducted, using a hybrid fluid-kinetic model [21] of the JOREK code [17] in which both the neutral particles and impurities are described by a full-f kinetic model coupled to the background plasma treated as fluid. It was shown that the model is able to capture XPR formation. Additionally, two phenomena were observed and analyzed. One was the formation of the high-field-side high-density (HFSHD) [13] due to the effect of kinetic neutrals, and the loss of it after the XPR formed. The other was complete detachment during the XPR formation, meaning that the heat flux onto the divertor target was strongly reduced [30] and showing that the XPR regime is inherently a detached regime. After the XPR formation, the XPR was successfully kept quasi-stationary with specific conditions of nitrogen seeding rate and deuterium fueling rate. Lastly, using the quasi-stationary XPR solution as a reference, the simulation was also continued with modified settings for the impurity seeding to investigate the dynamic response of the XPR. These correspond to the "high seeding case" with an increased nitrogen seeding rate Γ_{N_2} and the "retreating case" with nitrogen seeding being turned off.

In the reference case, the XPR core and the upper edge of the XPR were analyzed. The XPR core located at the peak of the impurity line radiation P_{rad}, where the local electron temperature T_X around 1 eV and a high nitrogen number density n_{imp} were observed. On the other hand, the upper edge of the XPR corresponded to a temperature of about 20 eV and marked the separation between high and low P_{rad}. Below this upper edge, the XPR access parameter X_A and n_{imp} rapidly increased. Additionally, the ionization front appeared to be at the upper edge, whilst volumetric recombination took place in the XPR core. Furthermore, the simulation showed an electric potential well in the XPR core and a thin potential hill above the XPR, and the resulting $E \times B$ transport lead to a stronger poloidal extension of the XPR core towards the IMP.

In the high seeding case, the upwards vertical development of the XPR and the MARFE formation were analyzed. As the XPR developed upwards, the following pattern was observed: high-density of the impurities extended towards the upper edge of the XPR $\mapsto$ radiation peak moved upwards and further cooled down the ionization front $\mapsto$ ionization front moved upwards $\mapsto$ a new XPR solution with larger vertical distance from the x-point to the radiation peak. Upon further increase of n_{imp} in the XPR, the XPR developed into a MARFE. In the MARFE scenario, the XPR core cooled down to around 0.03 eV, leading to an increase of recombination rate and the MARFE occurence parameter M_A locally.

In the retreating case, the downwards vertical development and the loss of the XPR were analyzed. As

the XPR developed downwards, the following pattern was observed: n_{imp} decreased in the XPR core $\mapsto$ radiation peak moved downwards and its intensity decreased $\mapsto$ ionization rate of deuterium neutral particles increased in the XPR core to maintain the power balance $\mapsto$ ionization front moved below the radiation peak $\mapsto$ decrease of neutral deuterium density $n_{D,neutral}$ lead to a local reduction of X_A $\mapsto$ a new XPR solution with smaller vertical distance from the x-point to the radiation peak. Eventually, as the neutral deuterium content in the XPR core was depleted from ionization, the XPR was lost although n_{imp} was not further decreased. Additionally, the loss of the electric potential well appeared to follow the decrease of n_{imp}.

In conclusion, this thesis work demonstrated the first axisymmetric JOREK XPR simulation that could be kept quasi-stationary. Additionally, the XPR solution could be varied by changing Γ_{N_2}, and the development of the XPR was analyzed through time. Towards the end, the simulation with increased Γ_{N_2} showed a MARFE formation, and the one with decreased Γ_{N_2} showed a loss of the XPR. For future work, these simulations provide a solid baseline for further developments as follows:

- Including additional physics processes such as neoclassical transport for impurities to capture impurity transport more accurately.
- Improving the setup for one-to-one experiment comparisons. This includes accurate setup of diffusivities and sources in order to match outer midplane profiles with experimental measurement.
- Studying the pressure balance in the evolution from XPR to MARFE, including all contributions from background plasma, kinetic neutrals, kinetic impurities and plasma flows.
- Transitioning to 3D simulations, for studying the mutual interaction between MHD instabilities and the atomic physics phenomena. This includes investigating the XPR dynamics across an ELM cycle, the suppression of ELMs by the XPR, and the MHD activity arising in the MARFE scenario. In this respect, also the effect of MHD activities on impurity transport is an important subject.

7 Acknowledgements

As my master's thesis project comes to an end, I would like to express my overflowing gratitude for having had all the opportunities and encounters at TUM and IPP Garching, specifically in the JOREK group. Although it is impossible to fully contain my gratitude in this chapter, I hope this shows the reader how nice and friendly the environment in this research field and institute is.

First of all, I would like to thank professor Stroth for giving amazing lectures on plasma physics, which got me into the exciting research field on fusion plasmas. As someone who has worked as a teacher before, I especially understand and appreciate the importance of good courses on guiding students to the right paths.

In the JOREK group, I would like to first thank Andrés and Matthias for all the help and guidance. With your hard work, our working group, and the JOREK group as a whole, provide a comfortable working environment where everyone is very well connected. Also, I have to especially thank Andrés and Sven for helping me learn to run JOREK and to use the kinetic particle extension in the beginning of this project. It was a steep leaning curve, and I would not have done it without your help. I cannot express how much I appreciate you two for being so patient and supportive.

As for my amazing colleagues, I definitely have to mention Felix first, for you found and fixed the major bug on fix_axis_nodes. This bug fix basically saved my life. Máté and Daniël, it was a great pleasure to work with you two on closely related topics. All the discussions and helping each other were really crucial elements for the success in this project. Besides collaboration in work, there were also the socializing activities, which helped me maintain the work-life balance during my studies. A really big thank you to all the members of the L7 group, for it has been so much fun being around you all.

Outside the JOREK group, I would like to especially thank Matthias Bernert, Konrad and Ou for all the fruitful discussions. It was absolutely essential for me to learn more about the XPR from the experimental side. To learn from other codes, the comparison with GRILLIX helped me gain insights on transport from turbulence, and it was very useful for me to learn how the XPR simulations were set up in SOLPS-ITER.

All of the memories I have made in the JOREK group and in the Max Planck Institute for Plasma Physics are extraordinarily precious, and I hope to still make a lot more of them in the future!

Acronyms

AUG	ASDEX Upgrade
CX	Charge exchange
ECRH	Electron cyclotron resonance heating
ELM	Edge localized mode
FW	First wall
HFS	High-field-side
HFSHD	High-field-side high-density
IMP	Inboard midplane
IT	Inner divertor
LFS	Low-field-side
LOS	Line of sight
MARFE	Multifaceted asymmetric radiation from the edge
MCF	Magnetic confinement fusion
MHD	Magnetohydrodynamics
NBI	Neutral beam injection
OMP	Outboard midplane
OT	Outer divertor
PFC	Plasma facing component
PFR	Private flux region

RMP	Resonant magnetic perturbations
SN	Single null
SOL	Scrape-off-layer
SOLPS	Scrape-off layer plasma simulation
XPR	X-point radiator

Bibliography

[1] R. Balescu. *Transport processes in plasmas. Pts. 1 and 2*. Elsevier Science Publisher B.V., Jan. 1988. ISBN: 0-444-87092-X.

[2] M. Bernert, F. Janky, B. Sieglin, A. Kallenbach, B. Lipschultz, F. Reimold, M. Wischmeier, M. Cavedon, P. David, M.G. Dunne, M. Griener, O. Kudlacek, R.M. McDermott, W. Treutterer, E. Wolfrum, D. Brida, O. Février, S. Henderson, M. Komm, the EUROfusion MST1 team, and the ASDEX Upgrade team. "X-point radiation, its control and an ELM suppressed radiating regime at the ASDEX Upgrade tokamak." In: *Nuclear Fusion* 61.2 (Dec. 2020), p. 024001. DOI: 10.1088/1741-4326/abc936. URL: https://dx.doi.org/10.1088/1741-4326/abc936.

[3] M. Bernert, S. Wiesen, O. Février, A. Kallenbach, J.T.W. Koenders, B. Sieglin, U. Stroth, T.O.S.J. Bosman, D. Brida, M. Cavedon, P. David, M.G. Dunne, S. Henderson, B. Kool, T. Lunt, R.M. McDermott, O. Pan, A. Perek, H. Reimerdes, U. Sheikh, C. Theiler, M. van Berkel, T. Wijkamp, and M. Wischmeier. "The X-Point radiating regime at ASDEX Upgrade and TCV." In: *Nuclear Materials and Energy* 34 (2023), p. 101376. ISSN: 2352-1791. DOI: https://doi.org/10.1016/j.nme.2023.101376. URL: https://www.sciencedirect.com/science/article/pii/S2352179123000157.

[4] J.P. Boris. "Relativistic plasma simulation-optimization of a hybrid code." In: *Proceeding of Fourth Conference on Numerical Simulations of Plasmas* (Nov. 1970).

[5] M. Cavedon, B. Kurzan, M. Bernert, D. Brida, R. Dux, M. Griener, S. Henderson, E. Huett, T. Nishizawa, T. Lunt, O. Pan, U. Stroth, M. Wischmeier, E. Wolfrum, and the ASDEX Upgrade Team. "Experimental investigation of L- and H-mode detachment via the divertor Thomson scattering at ASDEX Upgrade." In: *Nuclear Fusion* 62.6 (Apr. 2022), p. 066027. DOI: 10.1088/1741-4326/ac6071. URL: https://dx.doi.org/10.1088/1741-4326/ac6071.

[6] A.V. Chankin, D.P. Coster, R. Dux, Ch. Fuchs, G. Haas, A. Herrmann, L.D. Horton, A. Kallenbach, M. Kaufmann, Ch. Konz, K. Lackner, C. Maggi, H.W. Müller, J. Neuhauser, R. Pugno, M. Reich, and W. Schneider. "SOLPS modelling of ASDEX Upgrade H-mode plasma." In: *Plasma Physics and Controlled Fusion* 48.6 (May 2006), p. 839. DOI: 10.1088/0741-3335/48/6/010. URL: https://dx.doi.org/10.1088/0741-3335/48/6/010.

[7] O. Czarny and G.T.A. Huysmans. "Bézier surfaces and finite elements for MHD simulations." In: *Journal of Computational Physics* 227.16 (2008), pp. 7423–7445. ISSN: 0021-9991. DOI: https:

//doi.org/10.1016/j.jcp.2008.04.001. URL: https://www.sciencedirect.com/science/article/pii/S0021999108002118.

[8] G.L. Delzanno and E. Camporeale. "On particle movers in cylindrical geometry for Particle-In-Cell simulations." In: *Journal of Computational Physics* 253 (2013), pp. 259–277. ISSN: 0021-9991. DOI: https://doi.org/10.1016/j.jcp.2013.07.007. URL: https://www.sciencedirect.com/science/article/pii/S0021999113004798.

[9] ITER Physics Expert Group on Divertor, ITER Physics Expert Group on Divertor Modelling, Database, and ITER Physics Basis Editors. "Chapter 4: Power and particle control." In: *Nuclear Fusion* 39.12 (Dec. 1999), p. 2391. DOI: 10.1088/0029-5515/39/12/304. URL: https://dx.doi.org/10.1088/0029-5515/39/12/304.

[10] J.F. Drake. "Marfes: Radiative condensation in tokamak edge plasma." In: *The Physics of Fluids* 30.8 (Aug. 1987), pp. 2429–2433. ISSN: 0031-9171. DOI: 10.1063/1.866133. eprint: https://pubs.aip.org/aip/pfl/article-pdf/30/8/2429/12672634/2429_1_online.pdf. URL: https://doi.org/10.1063/1.866133.

[11] T. Eich, B. Sieglin, A.J. Thornton, M. Faitsch, A. Kirk, A. Herrmann, and W. Suttrop. "ELM divertor peak energy fluence scaling to ITER with data from JET, MAST and ASDEX Upgrade." In: *Nuclear Materials and Energy* 12 (2017). Proceedings of the 22nd International Conference on Plasma Surface Interactions 2016, 22nd PSI, pp. 84–90. ISSN: 2352-1791. DOI: https://doi.org/10.1016/j.nme.2017.04.014. URL: https://www.sciencedirect.com/science/article/pii/S2352179116302927.

[12] Ph. Ghendrih, K. Bodi, H. Bufferand, G. Chiavassa, G. Ciraolo, N. Fedorczak, L. Isoardi, A. Paredes, Y. Sarazin, E. Serre, F. Schwander, and P. Tamain. "Transition to supersonic flows in the edge plasma." In: *Plasma Physics and Controlled Fusion* 53.5 (Apr. 2011), p. 054019. DOI: 10.1088/0741-3335/53/5/054019. URL: https://dx.doi.org/10.1088/0741-3335/53/5/054019.

[13] D. Hachmeister, C. Silva, J. Santos, G. Conway, L. Gil, A. Silva, U. Stroth, J. Vicente, E. Wolfrum, R. McDermott, R. Dux, D. Brida, R. Fischer, and B. Kurzan. "Influence of the magnetic configuration on the high-field side scrape-off layer at ASDEX Upgrade and the role of the secondary separatrix." In: *Plasma Physics and Controlled Fusion* 66 (Apr. 2024). DOI: 10.1088/1361-6587/ad3a9f.

[14] C. Ham, A Kirk, S. Pamela, and H. Wilson. "Filamentary plasma eruptions and their control on the route to fusion energy." In: *Nature Reviews Physics* 2 (Mar. 2020), pp. 159–167. DOI: 10.1038/s42254-019-0144-1.

[15] S. Henderson, M. Bernert, D. Brida, M. Cavedon, P. David, R. Dux, O. Février, A. Järvinen, A. Kallenbach, M. Komm, R. McDermott, and M. O'Mullane. "Divertor detachment and reattachment with mixed impurity seeding on ASDEX Upgrade." In: *Nuclear Fusion* 63 (June 2023). DOI: 10.1088/1741-4326/ace2d6.

[16] M. Hoelzl, G.T.A. Huijsmans, F.J. Artola, E. Nardon, M. Becoulet, N. Schwarz, A. Cathey, S.J.P. Pamela, K. Aleynikova, F. Antlitz, V. Bandaru, H. Bergström, A. Bhole, T. Bogaarts, D. Bonfiglio, F. Cipolletta, T. Driessen, L. Edes, S. Futatani, G. Hao, F. Hindenlang, I. Holod, D. Hu, S. Hu, N. Isernia, H. Isliker, S.K. Kim, M. Kong, S. Korving, L. Kos, I. Krebs, S.J. Lee, Y.C. Liang, Z. Liang, S.J. Liu, Z.X. Lu, L. Meier, L. Messfeldt, V. Mitterauer, N. Nikulsin, B. Nkonga, R. Ramasamy, J. Reinking, C. Rogge, G. Rubinacci, K. Särkimäki, T. Smits, C. Sommariva, R. Sparago, K. Strien, M. Szucs, W. Tang, J. van Tongeren, F. Vannini, S. Ventre, F. Villone, C. Wang, L. Wang, F. Wieschollek, F. Wouters, J. Zielinski, and H. Zhang. "Non-linear MHD modelling of transients in tokamaks: a review of recent advances with the JOREK code." In: *Nuclear Fusion* 64.11 (Sept. 2024), p. 112016. DOI: 10.1088/1741-4326/ad5a21. URL: https://dx.doi.org/10.1088/1741-4326/ad5a21.

[17] M. Hoelzl, G.T.A. Huijsmans, S.J.P. Pamela, M. Bécoulet, E. Nardon, F.J. Artola, B. Nkonga, C.V. Atanasiu, V. Bandaru, A. Bhole, D. Bonfiglio, A. Cathey, O. Czarny, A. Dvornova, T. Fehér, A. Fil, E. Franck, S. Futatani, M. Gruca, H. Guillard, J.W. Haverkort, I. Holod, D. Hu, S.K. Kim, S.Q. Korving, L. Kos, I. Krebs, L. Kripner, G. Latu, F. Liu, P. Merkel, D. Meshcheriakov, V. Mitterauer, S. Mochalskyy, J.A. Morales, R. Nies, N. Nikulsin, F. Orain, J. Pratt, R. Ramasamy, P. Ramet, C. Reux, K. Särkimäki, N. Schwarz, P. Singh Verma, S.F. Smith, C. Sommariva, E. Strumberger, D.C. van Vugt, M. Verbeek, E. Westerhof, F. Wieschollek, and J. Zielinski. "The JOREK non-linear extended MHD code and applications to large-scale instabilities and their control in magnetically confined fusion plasmas." In: *Nuclear Fusion* 61.6 (May 2021), p. 065001. DOI: 10.1088/1741-4326/abf99f. URL: https://dx.doi.org/10.1088/1741-4326/abf99f.

[18] G.T.A. Huysmans and O. Czarny. "MHD stability in X-point geometry: simulation of ELMs." In: *Nuclear Fusion* 47.7 (June 2007), p. 659. DOI: 10.1088/0029-5515/47/7/016. URL: https://dx.doi.org/10.1088/0029-5515/47/7/016.

[19] A. Kallenbach, R. Dux, J.C. Fuchs, R. Fischer, B. Geiger, L. Giannone, A. Herrmann, T. Lunt, V. Mertens, R. McDermott, R. Neu, T. Pütterich, S. Rathgeber, V. Rohde, K. Schmid, J. Schweinzer, W. Treutterer, and the ASDEX Upgrade Team. "Divertor power load feedback with nitrogen seeding in ASDEX Upgrade." In: *Plasma Physics and Controlled Fusion* 52.5 (Mar. 2010), p. 055002. DOI: 10.1088/0741-3335/52/5/055002. URL: https://dx.doi.org/10.1088/0741-3335/52/5/055002.

[20] S.Q. Korving. "MHD Simulations of Neutral and Impurity Transport in ELM-controlled Plasmas: with application to ITER." English. Proefschrift. Phd Thesis 1 (Research TU/e / Graduation TU/e). Applied Physics and Science Education, June 2024. ISBN: 978-90-386-6065-3.

[21] S.Q. Korving, G.T.A. Huijsmans, J.-S. Park, A. Loarte, and the JOREK team. "Development of the neutral model in the nonlinear MHD code JOREK: Application to E × B drifts in ITER PFPO-1 plasmas." English. In: *Physics of Plasmas* 30.4 (Apr. 2023). ISSN: 1070-664X. DOI: 10.1063/5.0135318.

[22] S.Q. Korving, V. Mitterauer, G.T.A. Huijsmans, A. Loarte, M. Hoelzl, the ASDEX-Upgrade team, and the JOREK team. "Simulation of neoclassical heavy impurity transport in ASDEX Upgrade with applied 3D magnetic fields using the nonlinear MHD code JOREK." English. In: *Physics of Plasmas* 31.5 (May 2024). ISSN: 1070-664X. DOI: 10.1063/5.0198299.

[23] J.D. Lawson. "Some Criteria for a Power Producing Thermonuclear Reactor." In: *Proceedings of the Physical Society. Section B* 70.1 (Jan. 1957), p. 6. DOI: 10.1088/0370-1301/70/1/303. URL: https://dx.doi.org/10.1088/0370-1301/70/1/303.

[24] B. Lipschultz, B. LaBombard, E.S. Marmar, M.M. Pickrell, J.L. Terry, R. Watterson, and S.M. Wolfe. "Marfe: an edge plasma phenomenon." In: *Nuclear Fusion* 24.8 (Aug. 1984), p. 977. DOI: 10.1088/0029-5515/24/8/002. URL: https://dx.doi.org/10.1088/0029-5515/24/8/002.

[25] T. Luda, C. Angioni, M.G. Dunne, E. Fable, A. Kallenbach, N. Bonanomi, P.A. Schneider, M. Siccinio, G. Tardini, The ASDEX Upgrade Team, and The EUROfusion MST1 Team. "Integrated modeling of ASDEX Upgrade plasmas combining core, pedestal and scrape-off layer physics." In: *Nuclear Fusion* 60.3 (Feb. 2020), p. 036023. DOI: 10.1088/1741-4326/ab6c77. URL: https://dx.doi.org/10.1088/1741-4326/ab6c77.

[26] Open ADAS. *Open Source Atomic Data and Analysis Structure*. Accessed: 2024-07-12. URL: http://open.adas.ac.uk/.

[27] S.J.P. Pamela, A. Bhole, G.T.A. Huijsmans, B. Nkonga, M. Hoelzl, I. Krebs, E. Strumberger, and JET Contributors. "Extended full-MHD simulation of non-linear instabilities in tokamak plasmas." In: *Physics of Plasmas* 27.10 (Oct. 2020), p. 102510. ISSN: 1070-664X. DOI: 10.1063/5.0018208. eprint: https://pubs.aip.org/aip/pop/article-pdf/doi/10.1063/5.0018208/18217213/102510_1_5.0018208.pdf. URL: https://doi.org/10.1063/5.0018208.

[28] O. Pan, M. Bernert, T. Lunt, M. Cavedon, B. Kurzan, S. Wiesen, M. Wischmeier, U. Stroth, and the ASDEX Upgrade Team. "SOLPS-ITER simulations of an X-point radiator in the ASDEX Upgrade tokamak." In: *Nuclear Fusion* 63.1 (Nov. 2022), p. 016001. DOI: 10.1088/1741-4326/ac9742. URL: https://dx.doi.org/10.1088/1741-4326/ac9742.

[29] S. Potzel. "Experimental classification of divertor detachment." PhD thesis. Bayreuth, 2012. URL: https://epub.uni-bayreuth.de/id/eprint/210/.

[30] S. Potzel, M. Wischmeier, M. Bernert, R. Dux, H.W. Müller, A. Scarabosio, and the ASDEX Upgrade Team. "A new experimental classification of divertor detachment in ASDEX Upgrade." In: *Nuclear Fusion* 54.1 (Nov. 2013), p. 013001. DOI: 10.1088/0029-5515/54/1/013001. URL: https://dx.doi.org/10.1088/0029-5515/54/1/013001.

[31] F. Reimold, M. Wischmeier, M. Bernert, S. Potzel, A. Kallenbach, H.W. Müller, B. Sieglin, U. Stroth, and the ASDEX Upgrade Team. "Divertor studies in nitrogen induced completely detached H-modes in full tungsten ASDEX Upgrade." In: *Nuclear Fusion* 55.3 (Feb. 2015), p. 033004. DOI: 10.1088/0029-5515/55/3/033004. URL: https://dx.doi.org/10.1088/0029-5515/55/3/033004.

[32] V. Rozhansky, E. Kaveeva, I. Senichenkov, D. Sorokina, E. Vekshina, D. Coster, P. McCarthy, and N. Khromov. "Current structure in the scrape-off layer of a tokamak in a quiescent state." In: *Plasma Physics and Controlled Fusion* 63.1 (Nov. 2020), p. 015012. DOI: 10.1088/1361-6587/abc63c. URL: https://dx.doi.org/10.1088/1361-6587/abc63c.

[33] P.C. Stangeby. "The Plasma Boundary of Magnetic Fusion Devices." In: *Series in Plasma Physics* 7 (Jan. 2000). DOI: 10.1201/9781420033328.

[34] U. Stroth. *Plasmaphysik. Phänomene, Grundlagen und Anwendungen*. ger. 2. Auflage. SpringerLink : Bücher. Berlin ; [Heidelberg]: Springer Spektrum, 2018. ISBN: 978-3-662-55236-0. DOI: 10.1007/978-3-662-55236-0. URL: http://dx.doi.org/10.1007/978-3-662-55236-0.

[35] U. Stroth, M. Bernert, D. Brida, M. Cavedon, R. Dux, E. Huett, T. Lunt, O. Pan, M. Wischmeier, and the ASDEX Upgrade Team. "Model for access and stability of the X-point radiator and the threshold for marfes in tokamak plasmas." In: *Nuclear Fusion* 62.7 (Apr. 2022), p. 076008. DOI: 10.1088/1741-4326/ac613a. URL: https://dx.doi.org/10.1088/1741-4326/ac613a.

[36] T.A.J. Tongeren. "Simulating the dynamics of deuterium and impurity puffing in a tokamak plasma towards the formation of an X-point radiator." English. MSc Thesis (Research TU/e / Graduation TU/e). Applied Physics and Science Education, Nov. 2023.

[37] D.C. van Vugt. "Nonlinear coupled MHD-kinetic particle simulations of heavy impurities in tokamak plasmas." English. Proefschrift. Phd Thesis 1 (Research TU/e / Graduation TU/e). Applied Physics and Science Education, July 2019. ISBN: 978-90-386-4811-8.

[38] F. Wagner, G. Becker, K. Behringer, D. Campbell, A. Eberhagen, W. Engelhardt, G. Fussmann, O. Gehre, J. Gernhardt, G. v. Gierke, G. Haas, M. Huang, F. Karger, M. Keilhacker, O. Klüber, M. Kornherr, K. Lackner, G. Lisitano, G.G. Lister, H.M. Mayer, D. Meisel, E.R. Müller, H. Murmann, H. Niedermeyer, W. Poschenrieder, H. Rapp, H. Röhr, F. Schneider, G. Siller, E. Speth, A. Stäbler, K.H. Steuer, G. Venus, O. Vollmer, and Z. Yü. "Regime of Improved Confinement and High Beta in Neutral-Beam-Heated Divertor Discharges of the ASDEX Tokamak." In: *Phys. Rev. Lett.* 49 (19 Nov. 1982), pp. 1408–1412. DOI: 10.1103/PhysRevLett.49.1408. URL: https://link.aps.org/doi/10.1103/PhysRevLett.49.1408.

[39] J. Wesson and D.J. Campbell. *Tokamaks*. Vol. 149. Oxford University Press, Oct. 2011. ISBN: 9780199592234.

[40] H. Zohm. "Edge localized modes (ELMs)." In: *Plasma Physics and Controlled Fusion* 38.2 (Feb. 1996), p. 105. DOI: 10.1088/0741-3335/38/2/001. URL: https://dx.doi.org/10.1088/0741-3335/38/2/001.

[41] H. Zohm, C. Angioni, E. Fable, G. Federici, G. Gantenbein, T. Hartmann, K. Lackner, E. Poli, L. Porte, O. Sauter, G. Tardini, D. Ward, and M. Wischmeier. “On the physics guidelines for a tokamak DEMO.” In: *Nuclear Fusion* 53 (June 2013), p. 073019. DOI: 10.1088/0029-5515/53/7/073019.